Synergistic effect between Co single atoms and nanoparticles enables selective synthesis of bio-based benzimidazoles

Baoyu Wang [a,b], Mingrui Li [a], Songdang Zhang [a], Hongguo Wu [a], Yuhe Liao [c,*], Hu Li [a,*]

[a] National Key Laboratory of Green Pesticide, Key Laboratory of Green Pesticide & Agricultural Bioengineering, Ministry of Education, State-Local Joint Laboratory for Comprehensive Utilization of Biomass, Center for R&D of Fine Chemicals, Guizhou University, Guiyang, Guizhou 550025, China
[b] Guangxi Key Laboratory of Green Chemical Materials and Safety Technology, Beibu Gulf University, Qinzhou 535011, China
[c] Guangzhou Institute of Energy Conversion, Chinese Academy of Sciences, Guangzhou 510640, China

ABSTRACT

Finite size effect is closely correlated with heterogeneous catalytic activity and selectivity as reducing the metal to a few nanometers, but may suffer from deficient active sites for cascade reactions. Here, a type of dual-size heterogeneous N-doped cobalt catalysts (Co$_{SAs-NPs}$/NC(n)) with the coexistence of Co single-atoms (Co-SAs) and Co nanoparticles (Co-NPs) were prepared for efficient synthesis of benzimidazoles (up to 91% yield) from 2-nitroanilines and bio-based alcohols via cascade hydrogen transfer-dehydrogenative cyclization. Experimental results and density functional theory calculations suggested that the bio-alcohol dehydrogenation mainly occurs at Co-SAs sites, while Co-NPs sites remarkably facilitate the subsequent reduction of nitro species, indicating the synergistic effect between Co-SAs and Co-NPs in the coupled hydrogen transfer process. The Co$_{SAs-NPs}$/NC(0.25) catalyst can be recycled and applied to a wide range of substrates (28 examples). This catalytic approach based on the metal size effect opens a new route for the direct upgrading of biomass feedstocks involving multiple reactions.

1. Introduction

Renewable biomass resources can be converted into biofuels, high-value chemicals, and functional materials as a result of the presence of different oxygen-containing functional groups [1,2]. Bio-alcohols are widely accessible bio-based platform molecules, such as furfuryl alcohol obtained by hydrogenation of furfural or decarbonylation of 5-hydroxy-methylfurfural [3], and benzyl alcohol derived from lignin, which can be used as precursors for pharmaceutical and chemical industries, and as important raw materials for resins, rocket fuels, and plasticizers [1,4]. It would be attractive to synthesize biologically active products from biomass-derived compounds owing to the high value of pharmaceuticals and the multiple functional groups in bio-based compounds [5]. N-containing cyclic compounds (particularly N-heterocycles) are one of the most studied compounds in the pharmaceutical sector [6]. However, classical methods for the production of N-heterocycles often yield a huge amount of waste due to the introduction of several functional groups during the synthesis process [7,8]. Instead, the inherent functional groups in bio-based alcohols enable the synthesis of N-heterocyclic scaffolds in a green and promising conversion way, likely with water as the only by-product [9,10].

Benzimidazoles and their derivatives, as important N-heterocyclic compounds, have extensive pharmacological properties and biological activities, making them of great significance in industry and academia [11,12]. Although a variety of synthetic methods for benzimidazole derivatives have been developed (Scheme 1), most of the raw materials are derived from non-renewable fossil resources. Typically, *o*-phenyl-enediamine is used as the starting reactant to produce benzimidazole derivatives via a Ladenburg ring-closure reaction with a carbonyl or carboxyl compound (Scheme 1a) [13,14]. These synthetic processes are usually limited by a strong acidic reaction medium [15]. The coupling of alcohols with *o*-phenylenediamine has been explored to access benz-imidazoles through the dehydrogenation of alcohols (Scheme 1b) [16, 17], in which noble metals or expensive intricate transition metal complexes were used as the catalysts. From a raw material point of view, the oxidative stability of *o*-phenylenediamine in air limits its utilization as a starting material [18]. Alternatively, it would be a feasible strategy to use the chemically stable starting material 2-nitroaniline instead of *o*-phenylenediamine to synthesize benzimidazoles through in-situ reduction and subsequent C−N coupling cyclization (Scheme 1c) [18,
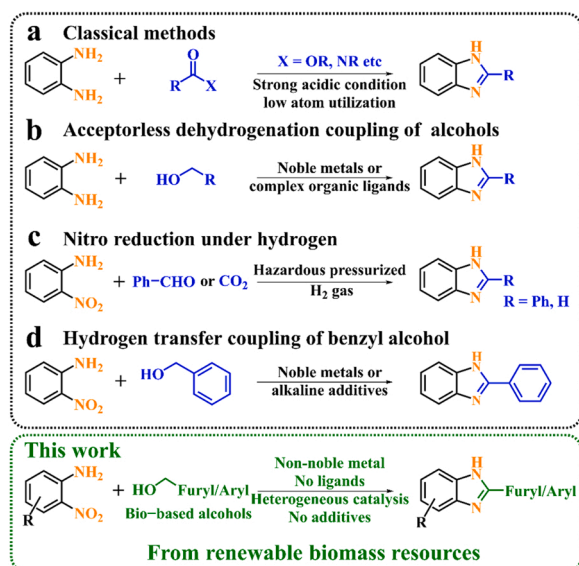
* Corresponding authors.
E-mail addresses: liaoyh@ms.giec.ac.cn, yuhe.liao20@gmail.com (Y. Liao), hli13@gzu.edu.cn (H. Li).

Scheme 1. Methods used for the synthesis of benzimidazole derivatives.

[19]. High H_2 pressure is typically used for the conversion of 2-nitroaniline to *o*-phenylenediamine [20,21]. The use of liquid alcohols instead of hydrogen as the hydrogen source has attracted attention with excellent redox economy for C−N bond coupling in combination with the hydrogen transfer process to yield benzimidazoles (Scheme 1d) [22,23]. Benzyl alcohol and its derivatives have been extensively studied due to the formation of more stable intermediates after dehydrogenation, yet in this reaction, either noble metal as a catalyst or base as an additive needs to be added to achieve high activity [24–34]. Generally, noble metals have higher H atom adsorption energy and moderate M−H bond energy, which are beneficial for H elimination on alpha carbon, hydrogen transfer, and hydrogen generation from alcohols [35–37]. Base metal catalysts are homogeneous or include complex and expensive organic ligands, as well as need homogeneous basic additives that favor dehydrogenation of alcohols and coupling of C−N bonds [38], which do not conform to the concept of green chemistry. In contrast, heterogeneous catalysts have obvious advantages in recovery and regeneration after reaction, accounting for more than 80% of current and historical applications [39,40]. From economic and environmental viewpoints, it is still desirable to develop highly active heterogeneous non-noble metal catalysts in the absence of an exogenous base for sustainable production of benzimidazoles from bio-based feedstocks via a hydrogen transfer-dehydrogenative cyclization strategy.

The metal catalysts with small particles generally exhibit superior catalytic performance due to the possibility of more exposed active sites [41,42]. When the particle size is reduced to the limit, it becomes isolated single-atom catalysts (SACs) [43]. With finely dispersed active sites and unique electronic structures, non-noble metal SACs exhibit high activity in many redox reactions, and are also one of the most promising materials to replace noble metals [44,45]. Although SACs have a strong ability to transfer electrons [46,47], one type of active site is more likely difficult to achieve satisfactory activity for complex cascade reactions, typically for the conversion of bio-based molecules [48]. This may originate from the competitive adsorption between substrate activation and H_2 dissociation, and isolated atoms can only provide limited adsorption sites [49]. In addition, due to the lack of metal−metal bonds in isolated atoms, H_2 is usually dissociated through a heterolytic dissociation pathway with a higher energy barrier, which greatly limits its hydrogenation reduction activity [48,50]. It can be expected that, according to the characteristics of complex cascade reactions, it is necessary to design and prepare catalytic materials with different metal sizes to obtain high performance.

In this work, a novel cobalt catalyst containing both Co-SAs and Co-NPs (nanoparticles) was prepared for the efficient production of bio-based benzimidazoles via a single-step hydrogen transfer-dehydrogenative cyclization method. This heterogeneous catalyst showed outstanding catalytic activity in the cascade dehydrogenation of bio-alcohols and reduction of nitro groups, which is comparable to or even superior to the activity of the noble metals. Both experimental results and DFT calculations suggested that the Co-SAs is a more efficient catalytically active sites for the dehydrogenation of bio-alcohols, while Co-NPs facilitate the reduction of nitro groups. This size-dependent catalytic strategy can provide a theoretical basis for the selective upgrading of biomass feedstocks via multi-step conversion processes.

2. Experimental

2.1. Materials

Cobalt nitrate hexahydrate (99%), zinc nitrate hexahydrate (99%), 2-methylimidazole (2-MeIm, 98%), terephthalic acid (99%), 2-nitroaniline (99%), *o*-phenylenediamine (99.5%), furfuryl alcohol (98%), furfural (99.5%), benzyl alcohol (99%), (5-methyl-2-furyl)methanol (97%), *N,N*-dimethylformamide (DMF, 99.5%), methanol (99.8%), chlorobenzene (99%), fuberidazole (98%), 2-phenylbenzimidazole, (98%), potassium thiocyanate (99%), potassium bicarbonate (99.5%), ammonium chloride (99.5%), and hydrochloric acid (37%) were purchased from Shanghai Aladdin Biochemical Technology Co., Ltd. All reagents were used directly without further purification unless otherwise noted.

2.2. Preparation of catalysts

2.2.1. Preparation of Co/ZIF(n) with different cobalt contents
The metal-organic framework materials with zeolite imidazoline framework (ZIF) were synthesized by thermal crystallization. In a typical procedure for preparation of Co/ZIF(n), methanolic solutions of cobalt nitrate hexahydrate and zinc nitrate hexahydrate in different molar ratios (6 mmol in total, 30 mL), and methanolic solutions of 2-MeIm (24 mmol, 30 mL) were mixed and stirred at room temperature for 1 h. Then, the mixture was transferred into a 100 mL stainless steel autoclave lined with Teflon and heated at 130 °C for 4 h. The as-obtained precipitates were centrifuged and washed with methanol several times and dried in vacuum at 80 ℃ overnight. The obtained precursors are coded as Co/ZIF(n) (n = 0, 0.08, 0.25, 0.5, and 1), where ***n*** is defined as the molar percentage of Co against total metals (Co and Zn) in the starting materials.

2.2.2. Preparation of Co$_{SAs-NPs}$/NC(n)
The dual-size heterogeneous N-doped cobalt catalysts (Co$_{SAs-NPs}$/NC (n)) were prepared by pyrolysis and Zn evaporation. In a general preparation procedure, the obtained powder of Co/ZIF(n) was placed in a tube furnace and then heated to the desired temperature at a heating rate of 5 °C·min^{-1} under an N_2 flow. Co/ZIF(n) was initially stayed at 150 °C for 1 h to remove the adsorbed water and organic solvent in ZIF, followed by stabilizing at 600 °C for 2 h to prevent the decomposition of the ligand (2-MeIm) to generate gas too fast and cause the collapse of catalyst. Then, considering the effect of pyrolysis temperature on the number of Co-SAs [51], the dispersion of Co was adjusted in the catalyst by evaporation of Zn at 900 °C for 2 h. Finally, the desired sample was obtained by cooling it to room temperature. The catalyst formed by Co/ZIF(0) with the absence of metallic Co is denoted as Free-Co/NC(0), and the Co/ZIF(0.08) exists in the form of Co-SAs after calcination (see the catalyst characterization section for details), denoted as Co$_{SAs}$/NC (0.08). Other Co/ZIF(n) materials with both Co-SAs and Co-NPs after calcination are denoted as Co$_{SAs-NPs}$/NC(0.25), Co$_{SAs-NPs}$/NC(0.5), and Co$_{SAs-NPs}$/NC(1), according to the difference of ***n***.
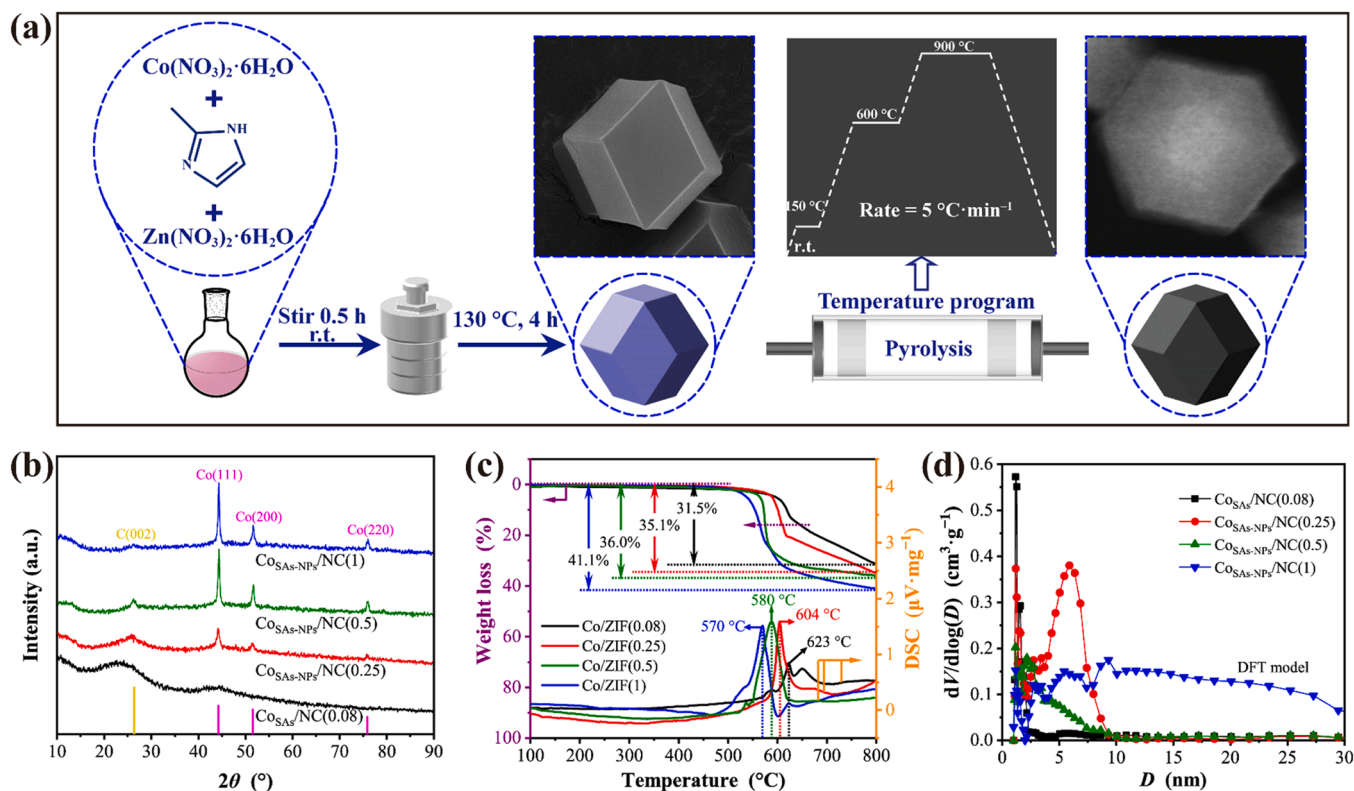
Fig. 1. (a) Schematic of the preparation of Co$_{SAs-NPs}$/NC(n). (b) XRD patterns, (c) TG-DSC curves, and (d) pore-size distributions of Co$_{SAs}$/NC(0.08), Co$_{SAs-NPs}$/NC (0.25), Co$_{SAs-NPs}$/NC(0.5), and Co$_{SAs-NPs}$/NC(1).

2.2.3. Preparation of Co$_{NPs}$@C

Typically, terephthalic acid (4 mmol) and cobalt nitrate hexahydrate (4 mmol) were dissolved in a round-bottom flask (250 mL) containing DMF (60 mL). Then, the round-bottom flask filled with the mixed solution was fitted with a reflux condenser and placed into an oil bath, and stirred at 120 °C for 8 h, followed by switching off the stirring and continuing to heating at the same temperature for 48 h. The centrifuged precipitate was washed three times with methanol and then placed in a vacuum oven at 60 °C overnight to obtain the metal-organic framework (MOF) precursor, which was further carbonized in a tube furnace at 900 °C to obtain the Co$_{NPs}$@C catalyst.

2.2.4. Preparation of Co/C

As a typical example, 100 mg of graphitic carbon powder was dispersed in 10 mL of cobalt nitrate methanol solution with a concentration of 100 mg·mL^{-1}, and sonicated at room temperature for 30 min. Then, the sample was centrifuged and vacuum-dried at 80 °C overnight. Finally, the obtained solid was reduced in a tube furnace under a hydrogen atmosphere (H$_2$/Ar = 1:9) at 550 °C for 4 h to obtain Co/C.

2.3. Catalyst characterization

The crystal structure of the samples was examined using a Bruker D8 X-ray diffractometer (XRD) (Cu target, Kα radiation, Ni filter, scanning range 5–90°). The thermogravimetric analysis and differential scanning calorimetry (TG-DSC) curves of the catalysts were obtained on an STA 449 F3 synchronous thermogravimetric analyzer (NETZSCH, Germany). The heating rate was 10 °C·min^{-1}, and the carrier gas was N$_2$. The pore structure was characterized using ASAP2400 static nitrogen automatic adsorption instrument (Micromeritics, USA). The elements and valence states of the samples were analyzed by an X-ray photoelectron spectrometer (XPS) (ESCALAB 250Xi, Thermo-Fisher). An 8×10^{-10} vacuum operating atmosphere and a monochromatic Al target were used, and the acceleration power was 15 kW, with a filament current of

16 mA. The test passing energy is 40 eV, the step size is 0.1 eV, and the charge correction is performed with the binding energy of C 1 s (284.60 eV) as the energy standard. The morphology of the samples was characterized by transmission electron microscopy (TEM) (FEI TALOS F200X) with an accelerating voltage of 200 kV. The aberration-corrected high-angle annular dark-field STEM (AC HAADF-STEM) images were acquired using Titan 80–300 and Titan Cubed Themis 60–300 scanning/transmission electron microscopes operating at 300 kV, equipped with probe spherical aberration correctors. The metal content of the samples was tested by an inductively coupled plasma instrument (ICP-OES 730, Agilent) after microwave digestion. The CO$_2$-TPD profiles of the catalysts were measured on an AutoChem II 2920 Chemisorber equipped with a thermal conductivity detector (TCD). The X-ray absorption fine structure (XAFS) spectra of Co K-edge were collected at 44 A beamline of the National Synchrotron Radiation Research Center (NSRRC, Taiwan). Lytle detector was used to collect data in fluorescence mode, and corresponding reference samples were gathered in transmission mode. The electrode sheet was first packaged on Kapton tape, and then the samples were ground and spread evenly on the special adhesive tape. All data obtained were processed according to standard procedures using the ATHENA module of the Demeter software package. For specific calculation details, see Supplementary Material.

2.4. Computational details

The first principle was employed to perform all density functional theory (DFT) calculations using the Perdew-Burke-Ernzerhof (PBE) formulation within a generalized gradient approximation (GGA). For specific computational details, see Supplementary material.
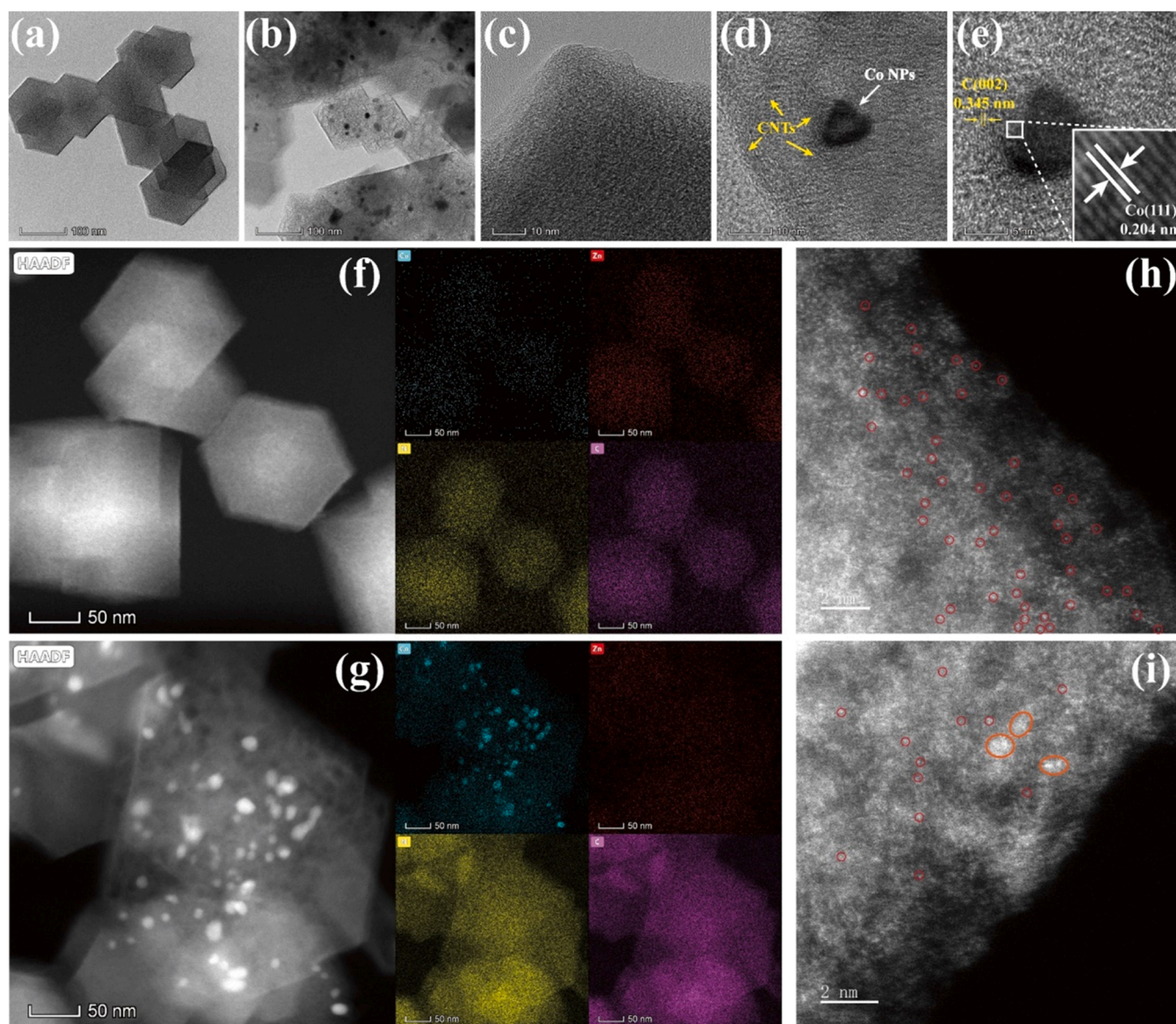
2.5. General procedures for the synthesis of benzimidazoles

All reactions were carried out in a stainless-steel autoclave (25 mL) with a magnetic stirrer. In a typical procedure, Co$_{SAs-NPs}$/NC(0.25)

Table 1

Characterization results of $Co_{SAs}/NC(0.08)$, $Co_{SAs-NPs}/NC(0.25)$, $Co_{SAs-NPs}/NC(0.5)$, and $Co_{SAs-NPs}/NC(1)$.

Catalyst	Specific area ($m^2 \cdot g^{-1}$)			Pore volume ($cm^3 \cdot g^{-1}$)			$D_{average}$[a]	Co ($wt\%$)[b]	Co ($wt\%$)[c]	Alkalinity ($mmol \cdot g^{-1}$)[d]
	S_{BET}[e]	S_{micro}[f]	S_{meso}[g]	V_{total}[h]	V_{micro}[i]	V_{meso}[j]				
$Co_{SAs}/NC(0.08)$	487.1	398.8	88.3	0.282	0.213	0.069	2.31	2.16	2.65	1.05
$Co_{SAs-NPs}/NC(0.25)$	539.6	330.4	236.2	0.376	0.157	0.219	2.79	8.22	8.04	1.01
$Co_{SAs-NPs}/NC(0.5)$	279.9	96.2	183.6	0.292	0.050	0.242	4.48	20.20	18.37	0.67
$Co_{SAs-NPs}/NC(1)$	260.5	97.2	163.3	0.185	0.049	0.136	2.64	35.82	31.71	0.39

[a] $D_{average}$: average pore size.

[b] Calculated from the results of ICP-OES.

[c] Calculated from the results of EDS.

[d] Calculated from the results of CO_2-TPD.

[e] S_{BET}: BET specific surface area.

[f] S_{micro}: microporous specific surface area from t-plot method.

[g] S_{meso}: mesoporous specific surface area from difference between S_{BET} and S_{micro}.

[h] V_{total}: total pore volume.

[i] V_{micro}: microporous pore volume from t-plot method.

[j] V_{meso}: mesoporous pore volume from difference between V_{total} and V_{micro}.

Fig. 2. STEM images of $Co_{SAs}/NC(0.08)$ (a) and $Co_{SAs-NPs}/NC(0.25)$ (b). HR-TEM images of $Co_{SAs}/NC(0.08)$ (c) and $Co_{SAs-NPs}/NC(0.25)$ (d, e). EDS elemental mappings of $Co_{SAs}/NC(0.08)$ (f) and $Co_{SAs-NPs}/NC(0.25)$ (g). AC HAADF-STEM images of $Co_{SAs}/NC(0.08)$ (h) and $Co_{SAs-NPs}/NC(0.25)$ (i).
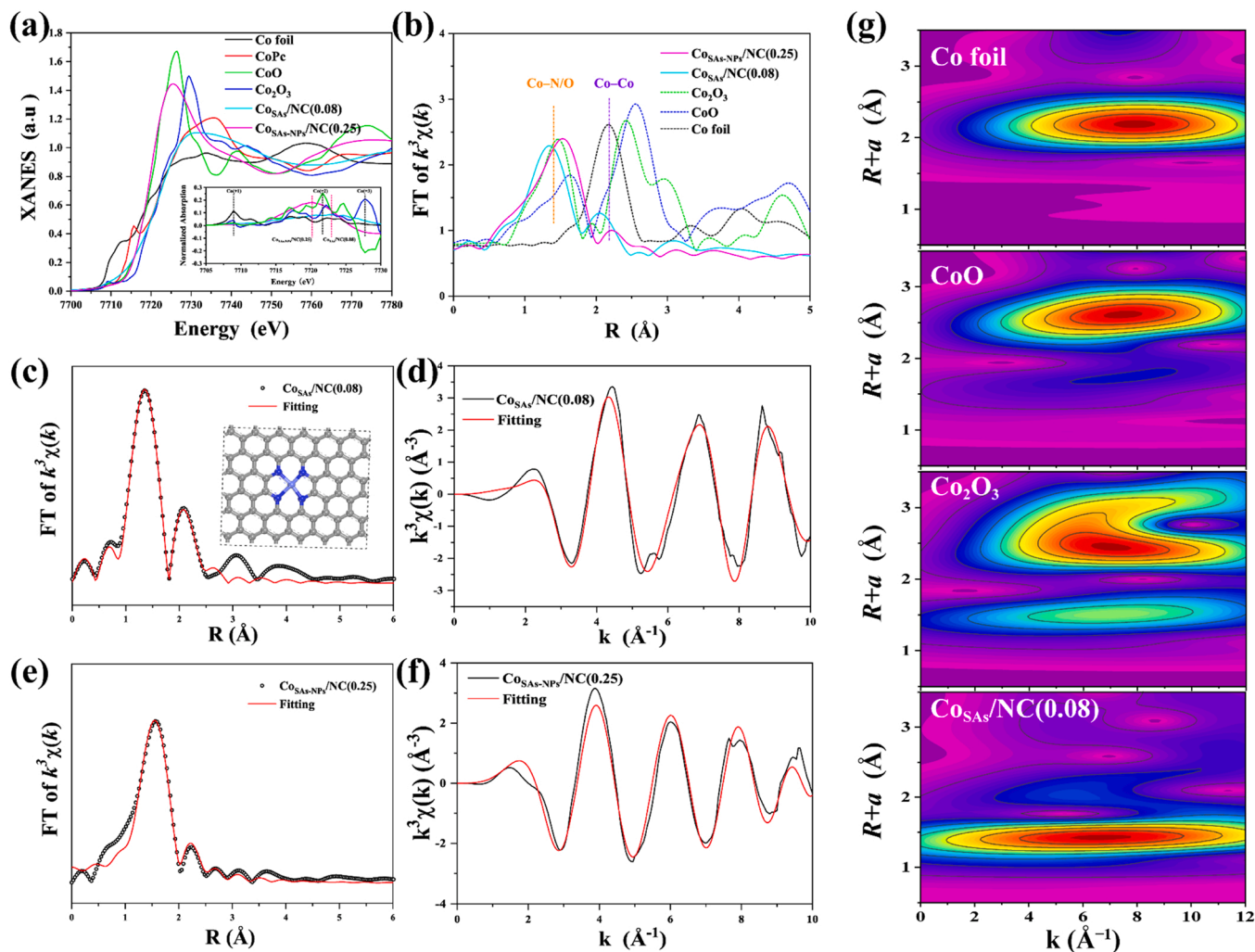
Fig. 3. Structural characterizations of $Co_{SAs}/NC(0.08)$ and $Co_{SAs-NPs}/NC(0.25)$ by XAFS spectroscopy. (a) K-edge XANES spectra and first derivative curves (insets) of $Co_{SAs}/NC(0.08)$, $Co_{SAs-NPs}/NC(0.25)$, and standard samples (Co foil, CoO, and Co_2O_3), (b) Fourier transformed magnitudes of the experimental K-edge EXAFS signals of $Co_{SAs}/NC(0.08)$ and $Co_{SAs-NPs}/NC(0.25)$ along with standard samples (underlines), (c) and (d) Co K-edge EXAFS analysis of $Co_{SAs}/NC(0.08)$ in R (c) and k (d) spaces, (e) and (f) Co K-edge EXAFS analysis of $Co_{SAs-NPs}/NC(0.25)$ in R (c) and k (d) spaces, (g) wavelet transform of the Co K-edge.

(0.025 mmol Co), furfuryl alcohol (3 mmol), 2-nitroaniline (0.5 mmol), and chlorobenzene (2 mL) were added to the reactor. It should be noted that the obtained activity was found to be within error for the reaction using the solvent in an increased volume (3, 5, and 8 mL), indicating that the volume difference did not affect the experimental results in this study. N_2 was slowly purged into the autoclave 3 times to displace the air inside the reactor. The reaction was carried out at 150 °C for 1–24 h under autogenous pressure. After the reaction, the mixture in the reactor was then analyzed by GC (Agilent 7890 A), equipped with an Agilent J&W HP-5 capillary column (30 m × 0.25 mm × 0.25 μm) and a flame ionization detector (FID) and GC/MS (Agilent 6890 N GC and 5973 MS). The oven was initially held at 60 °C for 1 min, then ramped to 240 °C at a rate of 10 °C·min^{-1}, and held for 10 min. Nitrogen was used as the carrier gas, and naphthalene was used as the internal standard substance. The turnover frequency (TOF) was calculated using Eq. (1) at low conversion (less than 30%) rates. In addition, information on the product's isolation, purification, and characterization can be found in the Supplementary Material.

$$TOF\ (h^{-1}) = \frac{Converted\ amount\ of\ feedstock\ (mmol)}{Total\ amount\ of\ Co\ in\ the\ catalyst\ (mmol)\ \times\ Time\ (h)}$$

(1)

3. Results and discussion

3.1. Synthesis and characterization of catalysts

Fig. 1a shows the schematic illustration of preparing Co/ZIF(n) precursors by thermal treatment and pyrolysis. The XRD patterns (Fig. S1) of all the ZIF precursors are in good agreement with the sodalite structure [52]. With the increase of Co content in the samples, the diffraction intensity shows a decreasing trend as Co is fluorescent with Cu radiation. This leads to an effective loss in the number of X-ray photons, thus lowering the diffraction intensities, and causing the systematic decrease of peak intensities with the increase of the Co/Zn ratio [53]. The dual-size N-doped cobalt catalysts ($Co_{SAs-NPs}/NC(n)$) were prepared from the ZIF precursors by temperature-programmed pyrolysis under nitrogen flow (Fig. 1a), and the XRD patterns of the calcined samples are shown in Fig. 1b. The diffraction peaks at $2\theta = 44.2$, 51.5 and 75.9° of $Co_{SAs-NPs}/NC(0.25)$, $Co_{SAs-NPs}/NC(0.5)$, and $Co_{SAs-NPs}/NC$ (1) samples can point to the (111), (200) and (220) planes of metallic cobalt, respectively. Only two broad peaks at 25° and 44°, corresponding to the (002) and (101) crystal plane diffractions of amorphous carbon, are observed for $Co_{SAs}/NC(0.08)$ [54]. With the increase of Co content, the (002) diffraction peaks are significantly shifted toward 26°, suggesting the formation of a graphitic carbon structure. The
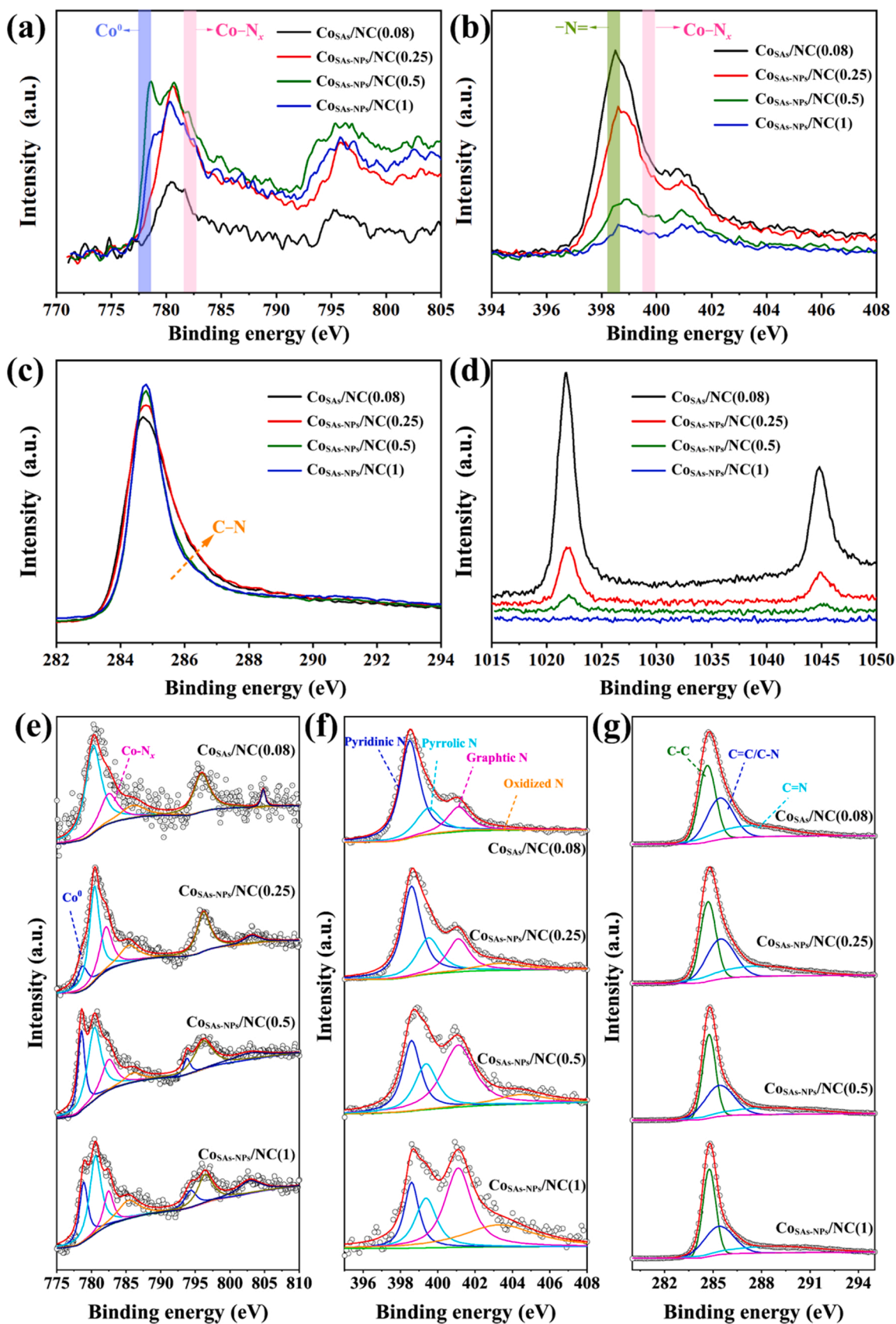
Fig. 4. High-resolution XPS spectra of Co$_{SAs}$/NC(0.08), Co$_{SAs-NPs}$/NC(0.25), Co$_{SAs-NPs}$/NC(0.5), and Co$_{SAs-NPs}$/NC(1). (a) Co 2p, (b) N 1 s, (c) C 1 s, and (d) Zn 2p, and deconvoluted XPS spectra of Co$_{SAs}$/NC(0.08), Co$_{SAs-NPs}$/NC(0.25), Co$_{SAs-NPs}$/NC(0.5), and Co$_{SAs-NPs}$/NC(1). (e) Co 2p; (f) N 1 s; (g) C 1 s.

characteristic diffraction peaks associated with ZnO are not observed in the calcined samples, and likely the ZnO exists in an amorphous or highly dispersed form. The TG curves show that the total weight loss of Co/ZIF(0.08) at 800 °C is 31.5%, which is nearly 10% lower than that of Co/ZIF(1) (Fig. 1c). Meanwhile, with the decrease of the Zn doping ratio (i.e., increase of the cobalt content), the samples began to lose weight rapidly at lower temperatures. Particularly, the endothermic peak of Co/ZIF(0.08) determined by differential scanning calorimetry (DSC) appeared at 623 °C, which was higher than that of Co/ZIF(1) (570 °C). This is because the coordination ability of 2-MeIm with Zn^{2+} is stronger than that with Co^{2+}, which leads to the decomposition of 2-MeIm in Co/ZIF(1) at a lower temperature [55].

The structural and textural properties of $Co_{SAs-NPs}/NC(n)$ were studied by N_2 adsorption-desorption isotherms (Fig. S2), and the obtained results are shown in Table 1. The sharp uptakes of Co_{SAs}/NC (0.08) and $Co_{SAs-NPs}/NC(0.25)$ at a low relative pressure indicated the existence of a large number of micropores. The hysteresis loops at a relative pressure ranging from 0.45 to 1.0, which are caused by the capillary condensation of N_2 in the mesopores with a wide size distribution, are more distinct in the $Co_{SAs-NPs}/NC(0.25)$, $Co_{SAs-NPs}/NC(0.5)$, and $Co_{SAs-NPs}/NC(1)$ samples. The increase in the number of mesopores makes the S_{meso} of these samples larger than that of $Co_{SAs}/NC(0.08)$ (88.3 $m^2 \cdot g^{-1}$), and their V_{meso} and $D_{average}$ increase as well, compared with $Co_{SAs}/NC(0.08)$ (Table 1). These mesopores are mainly caused by the dislocation of metal cobalt from the original organic ligand during the carbonization process. As the Zn contents of the calcined samples decreased, more Co atoms were aggregated in the mesopores, resulting in the results of the S_{meso}, V_{meso}, and $D_{average}$ all having a trend of volcano curve. However, the sharp decrease from 539.6 $m^2 \cdot g^{-1}$ to 260.5 $m^2 \cdot g^{-1}$ in the S_{BET} of the samples with high cobalt contents is mainly due to the collapse of the original microporous structure caused by the graphitization of amorphous carbon [54]. In short, the $Co_{SAs-NPs}/NC(n)$ catalyst with an appropriate cobalt content has a hierarchical pore structure, as evidenced by the pore size distribution (Fig. 1d).

TEM shows the overall polyhedral-like morphology of the carbonized $Co_{SAs-NPs}/NC(n)$ (Fig. 2a & b). Notably, no spots representing metal nanoparticles were found in Free-Co/NC(0) and $Co_{SAs}/NC(0.08)$ compared to $Co_{SAs-NPs}/NC(0.25)$ at the scale of 100 nm. Meanwhile, elemental mappings showed that the Co element in $Co_{SAs}/NC(0.08)$ was highly dispersed (Fig. 2f and Figs. S3,4). Contrastly, the samples with a lower Zn original content in ZIF (< 75 mol%) resulted in severe Co agglomeration (Fig. 2g and Fig. S5). The $Co_{SAs}/NC(0.08)$ catalyst is directly observed from the aberration-corrected high-angle annular dark-field STEM (AC HAADF-STEM) image (Fig. 2h), which shows highly dispersed bright spots. These results indicate that the presence of high-content Zn species can effectively suppress Co sintering during carbonization due to the spatial isolation of Co by Zn elements. Besides, it can confirm that Co exists in the form of a single atom in the sample with a Co content of 2.16% (Table 1). Similar to the above results, bright spots representing single atoms also appeared in the AC HAADF-STEM image of the Free-Co/NC(0) (Fig. S6), suggesting the possibility of Zn-SAs in this sample. However, no bright spots representing Co-SAs were found in the AC HAADF-STEM image of the catalyst $Co_{NPs}@C$ prepared using the MOF precursor synthesized from terephthalic acid and Co^{2+} ions (Fig. S7). It can be speculated that the N element in the ligand is the root cause of the formation of Co-SAs. STEM and high-resolution TEM (HR-TEM) images show that $Co_{SAs-NPs}/NC(0.25)$ displays a structure of carbon nanotubes (CNTs) (Fig. 2b,d), confirming the transformation of the $Co_{SAs-NPs}/NC(n)$ samples from amorphous carbon to graphitic carbon with increasing the Co content. Fig. 2e shows that the lattice fringes of the embedded Co-NPs and the CNTs are 0.204 and 0.345 nm, corresponding to the face-centered cubic metallic Co(111) plane (PDF 15–0806) and C(002) plane (PDF 41–1487), respectively. HAADF-STEM and corresponding elemental mappings (Fig. 2g and Fig. S8) confirmed that C and N were uniformly distributed on the catalyst surface. As the

Co content increases, the Co-NPs become more aggregated and occupy the external specific surface area of the catalyst, leading to a significant decrease in the surface area (Table 1). As a comparison, the Co/C catalyst prepared by the impregnation method exists in the form of nanoparticles, and the metal particle size is not uniform (Fig. S9). The elemental content in the samples was roughly calculated by energy dispersive spectroscopy (EDS) and found that the $Co_{SAs}/NC(0.08)$ catalyst had a Co content of 2.65%. The ICP-OES measurement shows that the Co content of $Co_{SAs}/NC(0.08)$ is 2.16% (Table 1). These two results (i.e. EDS and ICP-OES) indicate the high dispersion of Co atoms on the $Co_{SAs}/NC(0.08)$ catalyst. In other samples with more Co present, the detected Co content using EDS was lower than the actual value, due to the agglomeration of Co particles (Table 1). The AC HAADF-STEM image of the $Co_{SAs-NPs}/NC(0.25)$ sample shows bright spots that represent Co-SAs (Fig. 2h), but the aggregated bright spots suggest the presence of Co nanoclusters or NPs (Fig. 2i).

To further determine the local chemical bonding of Co atoms, the catalysts were analyzed by XAFS Co K-edge containing the near-edge and extended energy regions (Fig. 3). The valence state of the metal in the catalyst can be revealed by the position of the absorption edge in the X-ray absorption near-edge structure (XANES) spectrum (Fig. 3a). Compared to the spectra obtained from standard samples including Co foil, cobalt phthalocyanine (CoPc), CoO, and Co_2O_3, $Co_{SAs}/NC(0.08)$ has a metallic Co valence similar to CoPc, which can be considered around + 2 (CoO). A comparison of the first derivative XANES for Co_{SAs}/NC (0.08) and $Co_{SAs-NPs}/NC(0.25)$ with references indicates that the latter shows a relatively lower valence state of Co (inset of Fig. 3a), which is mainly due to the presence of non-negligible zero-valent Co (Co-NPs) in the catalyst. Meanwhile, the pre-edge peaks in the Co K-edge XANES spectrum (~7710 eV) arise from the 1 s to 3d transition. Usually, the intensity of this peak in the K-edge spectrum of 3d metals is related to the degree of 3d-4p mixing, with increasing the pre-edge characteristic intensity and decreasing central symmetry of the metal coordination [56]. Compared with the cubic CoO reference sample, the pre-edge peak intensities of the $Co_{SAs}/NC(0.08)$ catalyst indicate that the coordination center symmetry of Co in the catalyst is lower than that of the cubic complex. The $Co_{SAs}/NC(0.08)$ and $Co_{SAs-NPs}/NC(0.25)$ catalysts were validated by quantitative least squares extended X-ray absorption fine structure (EXAFS) curve fitting analysis (Fig. 3b-f). The peaks located at ~1.4 Å for both catalysts correspond to the Co–N/O scattering path (Fig. 3b). Fitting using a single Co–N scattering path found that $Co_{SAs}/NC(0.08)$ and $Co_{SAs-NPs}/NC(0.25)$ had fitted coordination numbers of 3.9 ± 1.0 and 4.1 ± 3.1 in the first shell, respectively (Table S1). Combined with the centrosymmetric information given by the Co K-edge pre-edge characteristic intensity, it implies a square-pyramidal configuration for the Co–N bonding. Noting that the characteristic peak of the R space curve at 2.02 Å in the $Co_{SAs}/NC(0.08)$ catalyst can be attributed to the contribution of C atoms, the coordination number of 7.3 ± 2.5 (Table S1) implies the Co–N–C structure in the $Co_{SAs}/NC(0.08)$ (inset of Fig. 3c). In addition, the Co–Co peak at about 2.2 Å was not detected, indicating that Co metal is atomically dispersed (Fig. 3b & c). To further confirm the atomic dispersion of Co in the $Co_{SAs}/NC(0.08)$ catalyst, wavelet transform (WT) Co K-edge EXAFS was performed (Fig. 3g). WT analysis of the catalyst shows only one intensity maximum at about 6 $Å^{-1}$, which can be attributed to Co–N coordination. Unlike the characteristics of Co foil, CoO, and Co_2O_3 samples, the crystalline metal structure is completely absent in $Co_{SAs}/NC(0.08)$. Correspondingly, the second coordination layer of the $Co_{SAs-NPs}/NC(0.25)$ catalyst found a Co–Co scattering path (Fig. 3b & e), indicating the existence of Co clusters in the catalyst, which is consistent with the STEM results.

The chemical structure and bonding state of the samples were investigated by X-ray photoelectron spectroscopy (XPS). The $Co_{SAs-NPs}/NC(n)$ catalysts, except for $Co_{SAs-NPs}/NC(1)$, were found to be mainly composed of C, Co, Zn, and N elements (Fig. S10), consistent with the EDS results (Fig. S11). In the high-resolution XPS spectra of Co 2p

Table 2
The activity of Co catalysts with different metal sizes in transfer hydrogenative cyclization of 2-nitroaniline (**1a**) and bio-based furfuryl alcohol (**2a**) to **3a** and byproducts (**4a** & **5a**).

Entry	Catalyst	Conv. of **1a** (%)	Yield (%)			TOF $(h^{-1})^a$
			3a[b]	**4a**[b]	**5a**	
1	Free-Co/NC(0)	6.1	2.4 (1.3)	-	3.5	0.32
2[c]	Co$_{SAs-NPs}$/NC(0.25)	62.9	54.2 (46.9)	6.2 (2.5)	-	4.63
3	Co$_{SAs-NPs}$/NC(0.25)	100	86.8 (80.9)	4.3 (1.7)	-	7.58
4	Co$_{SAs}$/NC(0.08)	91.4	59.4 (51.1)	2.9 (0.9)	18.8	7.26
5	Co$_{SAs-NPs}$/NC(0.5)	17.4	2.7 (1.2)	8.9 (3.3)	3.1	1.75
6	Co$_{SAs-NPs}$/NC(1)	15.8	1.9 (0.6)	10.1 (3.9)	2.2	1.54
7	Co$_{SAs}$/NC(0.08)(KSCN)	87.5	52.1 (47.7)	1.3 (0.2)	19.4	6.92
8	Co$_{SAs-NPs}$/NC(0.25)(KSCN)	72.9	41.1 (37.1)	2.2 (0.5)	18.9	5.73

Reaction conditions: 0.025 mmol Co of catalyst, 0.5 mmol 1a, 3 mmol 2a, 150 °C, 10 h, 2 mL chlorobenzene.
[a] TOF was calculated based on the total amount of Co at low **1a** conversions (less than 30%).
[b] Isolated yields are in parentheses
[c] 1.5 mmol of **2a**.

(Fig. 4a), the samples with more than 25 mol% of Co added were observed to show a significant increase in the intensity at a binding energy of ~778.5 eV, indicating that a large number of Co-NPs (Co^0) were formed in these samples after calcination, consistent with the STEM results (Fig. S5). As the Co loading decreases, the Co^0 content is gradually brought down and the peak position shifts to the direction of high binding energy. After deconvolution of the Co 2p XPS spectrum (Fig. 4e), it was found that Co$_{SAs}$/NC(0.08) hardly contains the peak of Co^0 (Table S2), and the relative contents of Co−N$_x$ bonds in Co$_{SAs}$/NC (0.08) and Co$_{SAs-NPs}$/NC(0.25) are 18.05% and 20.00%, respectively, which are higher than those of Co$_{SAs-NPs}$/NC(0.5) and Co$_{SAs-NPs}$/NC(1). The N 1 s spectra indicate that the N content decreased significantly with the increase of Co content (Fig. 4b), this is similar to that reported in the literature [57,58]. This may be caused by the fact that Co/ZIF more likely undergoes dislocation to form Co-NPs after calcination, and then NH$_3$ is released from 2-MeIm coordinated with Co^{2+} at high-temperature calcination [59], thus leading to the reduction of N content. Fitting the N 1 s spectra with a Gaussian function and quantitative deconvolution of the overlapping peaks typically detected four N − states, including pyridine N (ca. 398.5 eV), pyrrolic N (ca. 399.6 eV), graphite N (ca. 401.3 eV), and oxidized N (ca. 403.0 eV) (Fig. 4f). With the increase of Co content, the decrease of the relative content of pyridine N and the increase of graphitic N in the sample can also indicate that Co is separated from the ligand and aggregated at a high temperature, which makes the sample more easily graphitized (Table S2), in good agreement with the XRD and BET characterization results (Fig. 1b, Table 1). The high-resolution C 1 s core-level spectra of the four samples had roughly the same curve shape, corresponding to carbon−nitrogen bonds with high binding energy (C−N, C=N) and carbon−carbon bonds with low binding energy (C−C, C=C) (Fig. 4c,g). The relative ratio of C−N bonds in Co$_{SAs-NPs}$/NC(n) decreasing with a high Co content can be ascribed to the decrease of N content in the material (Table S2). The Zn XPS spectra of the samples had two peaks at 1045 and 1022 eV near, assigned to Zn 2p$_{1/2}$ and Zn 2p$_{3/2}$ of ZnO, respectively (Fig. 4d), while the signal intensity decreases with the increase of Co content.

The alkalinity of the catalyst is measured by the chemisorption of the acid probe molecule CO$_2$ (Fig. S12). With the increase of Zn addition, the alkalinity of the catalyst gradually increased (Table 1). Due to the complex origin of alkalinity in the catalyst, it is difficult to separate the CO$_2$ desorption peaks one by one by deconvolution. To be sure, the source of alkalinity has the following components. (1) In the occupied region near the Fermi level, the carbon atoms adjacent to the pyridine N have a localized density of states, which leads to the possible generation of weak Lewis bases (100 °C $< T_m <$ 300 °C) in the electron pair donation of carbon atoms [60]. (2) The adsorption of CO$_2$ by zinc oxide at 200–300 °C can also produce the corresponding alkalinity [61]. (3) Carbon nanostructures containing pyridine N have strong Lewis basicity [62,63]. Overall, as shown by N 1 s XPS (Table S2), the increase of pyridine N content with the increase of Zn and the interaction of ZnO with Co-NPs lead to the increased basicity of the catalyst.

3.2. Catalytic activity test

In a preliminary study, catalytic transfer hydrogenative cyclization of 2-nitroaniline (**1a**) and bio-based furfuryl alcohol (**2a**) toward bio-based 2-(2-furyl)1*H*-benzimidazole (**3a**) was performed to evaluate the catalyst performance (Table 2). When Free-Co/NC(0) was used as the catalyst, a low yield of **3a** (2.4%) was obtained (entry 1, in Table 2), indicating that metal Zn was difficult to reduce the nitro group. Theoretically, 2 molecules of **2a** are required for each molecule of **1a** to be reduced. However, the undesired decomposition and condensation of **2a** will consume itself [64]. A certain amount of decomposition product (i. e., 2-methylfuran), self-etherification product (i.e., 2,2′-difurfuryl ether) of furfuryl alcohol, and the formaldehyde-deformation product (i.e., 2, 2′-methylenedifuran) of 2,2′-difurfuryl ether were observed by GC-MS (Fig. S13). In addition, the intermediates generated from **2a** in the hydrogen transfer reaction are unstable compared to benzyl alcohol, because the furan ring is less aromatic than the benzene ring [65]. Accordingly, a larger amount of **2a** is required in the reaction to obtain a better conversion of **1a**. When the molar ratio of **2a** and **1a** was 3:1, the maximum conversion of 2-nitroaniline was 62.9% (entry 2, in Table 2). With the molar ratio of 6:1 (**2a**:**1a**), the conversion of **1a** greatly increased and could be completed within 10 h (entry 3, in Table 2), and the equilibrium of furfuryl alcohol under GC yield was above 91% (Table S3). Therefore, the concentration of the hydrogen donor **2a** had an important effect on the conversion of **1a**. The turnover frequency (TOF) of Co$_{SAs}$/NC(0.08) was observed to be 22.7, 4.7, and 4.1 times higher than that of Free-Co/NC(0), Co$_{SAs-NPs}$/NC(1) and Co$_{SAs-NPs}$/NC (0.5), respectively, but slightly lower than that of Co$_{SAs-NPs}$/NC(0.25) (entries 1 & 3–6 in Table 2). The extrapolated initial reaction rate of Co$_{SAs-NPs}$/NC(0.25) was 3.46 × 10^{-5} mol·L^{-1}·s^{-1} (Table S4), which is
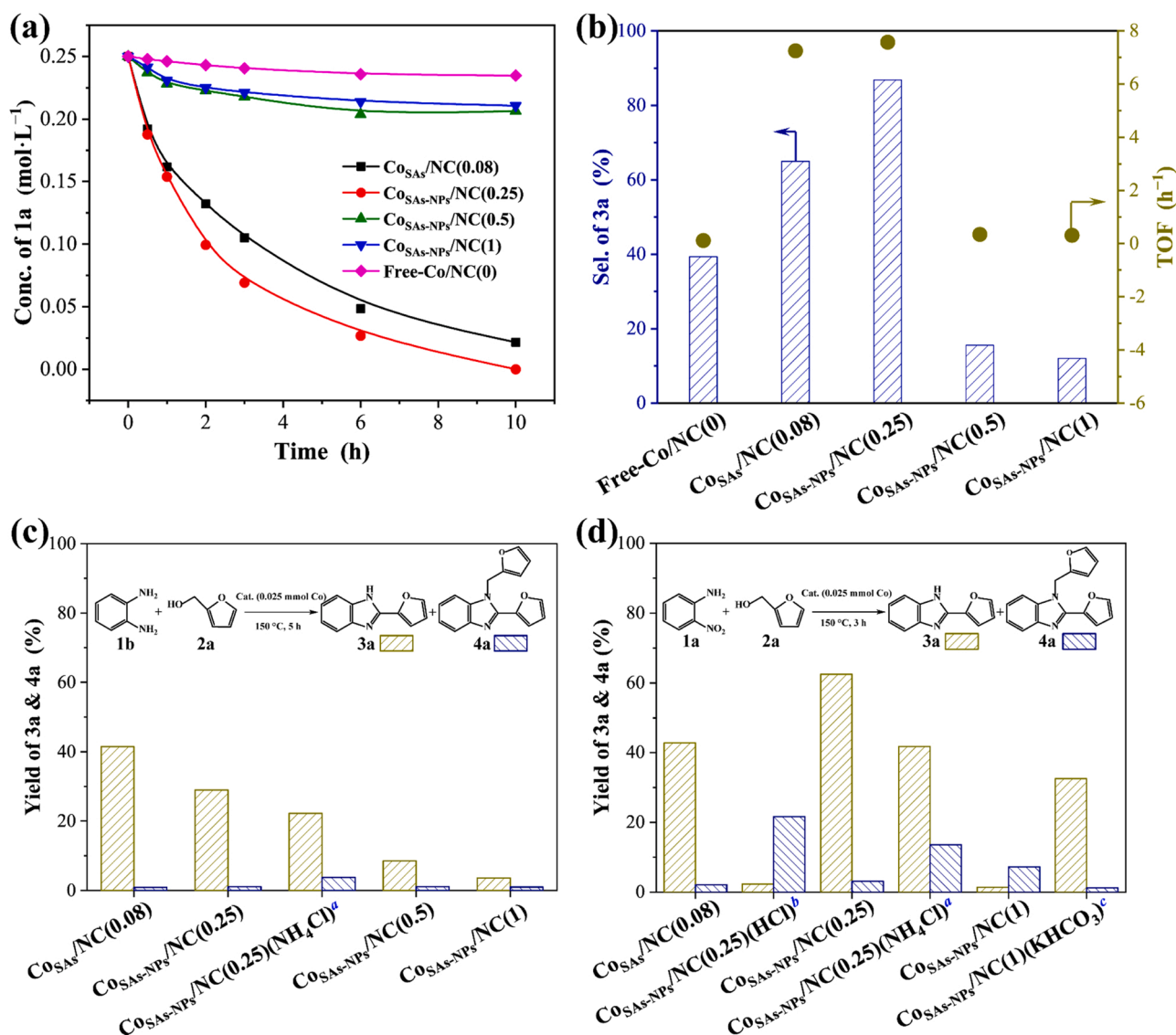
Fig. 5. (a) Kinetic curves for the conversion of **1a**. (b) Relationship between TOF and **3a** selectivity of the catalyst. (c) The activity of different Co catalysts for the reaction of *o*-phenylenediamine (**1b**) with **2a**, and (d) activity of different Co catalysts for the reaction of **1a** with **2a**. Reaction conditions: (a) 0.025 mmol Co of catalyst, 0.5 mmol **1a**, 3 mmol **2a**, 150 °C, 2 mL chlorobenzene. (c) 0.025 mmol Co of catalyst, 0.5 mmol *o*-phenylenediamine (**1b**), 3 mmol **2a**, 150 °C, 5 h, 2 mL chlorobenzene. (d) 0.025 mmol Co of catalyst, 0.5 mmol **1a**, 3 mmol **2a**, 150 °C, 3 h, 2 mL chlorobenzene. [a] 2 mmol of NH₄Cl. [b] Acid-etching conditions: 8 M HCl, 24 h, room temperature, 100 mg (catalyst)/10 mL HCl. [c] 1 mmol of KHCO₃.

4.9 and 7.2 times higher than that of $Co_{SAs-NPs}/NC(0.5)$ and $Co_{SAs-NPs}/NC(1)$, respectively. Meanwhile, Co/C and $Co_{NPs}@C$ catalysts also showed unqualified catalytic activity due to the low utilization of active sites caused by their relatively large metal particle size (Figs. S7 and S9). It should be noted that the catalytic activity of $Co_{SAs-NPs}/NC$ (0.23) and $Co_{SAs-NPs}/NC(0.27)$ is not much different from that of $Co_{SAs-NPs}/NC(0.25)$ (Fig. S14). This may be because the degree of dispersion of Co-NPs does not change much after slightly changing the Co content, thus not affecting its catalytic performance. Fig. 5a shows that the activity of the Free-Co catalyst is lower than that of other Co-based catalysts, implying the major role of metallic Co in this reaction. The activity of $Co_{SAs-NPs}/NC(0.25)$ is comparable to or even better than $Co_{SAs}/NC(0.08)$ although the latter is a single-atom catalyst, which is assumed to give the highest activity due to 100% atom utilization. Interestingly, the selectivity to **3a** is different between $Co_{SAs}/NC(0.08)$ and $Co_{SAs-NPs}/NC(0.25)$. For instance, it is shown that the yield of **3a** over $Co_{SAs}/NC(0.08)$ increased by 27% compared to $Co_{SAs-NPs}/NC(0.25)$ (entries 3 & 4 in Table 2). The formation rate of **3a** of $Co_{SAs-NPs}/NC(0.25)$ is 3.03×10^{-5} mol·L⁻¹·s⁻¹ (Table S3), which is 1.61 times higher than

that of $Co_{SAs}/NC(0.08)$. The above data suggest that the lower selectivity of SACs in this reaction (Fig. 5b), and the formation of side product **5a** is the main reason for the low selectivity of **3a**. However, **5a** was not detected in the presence of $Co_{SAs-NPs}/NC(0.25)$ with both Co-SAs and Co-NPs, indicating the transfer hydrogenative cyclization of **1a** with **2a** requires multiple active sites to obtain high selectivity. The conversion of **1a** after the physical mixing of $Co_{SAs}/NC(0.08)$ and Co/C is only 60.2%, which is 40% lower than that of the $Co_{SAs-NPs}/NC(0.25)$ catalyst (Fig. S14). In brief, neither $Co_{SAs}/NC(0.08)$ and Co/C catalysts nor the catalyst formed by the physical mixture of the two reached the optimal catalytic system. The low-metal loading of SACs in physically mixed catalysts often necessitates heavy loading of the total catalyst, worsening mass-transfer resistance [46]. Moreover, for the cascade hydrogen transfer reaction, alcohols and nitroaromatics are prone to be adsorbed on the Co-SAs and Co-NPs sites, respectively, and the resulting infranchissable spatial isolation is not favorable for the cascade reaction over different active sites. It can thus be speculated that the adjacent dual-size Co sites on the $Co_{SAs-NPs}/NC(0.25)$ catalyst have a synergistic effect on this cascade reaction to achieve an optimal catalytic system. It should be
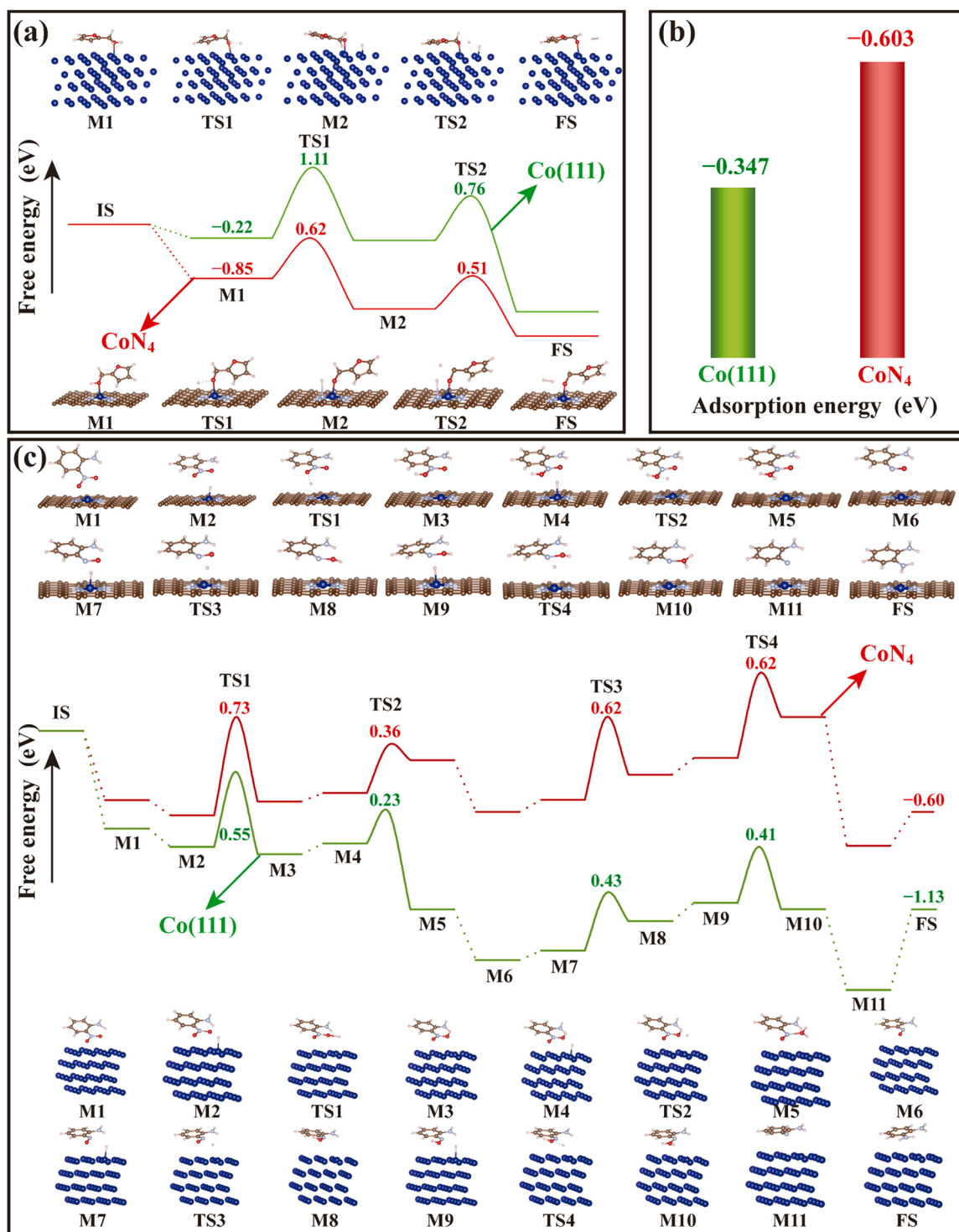
Fig. 6. (a) Reaction pathways and corresponding energy profiles of CoN$_4$ and Co(111) for the dehydrogenation of **2a**, (b) adsorption energy of H* on Co(111) and CoN$_4$ sites, and (c) partial reaction pathways and free energy profiles of CoN$_4$ and Co(111) for hydrogenation reduction of **1a**. Note: IS is initial state; M is intermediate; TS is the transition state; and FS is final state.

noted here that the selectivity difference is not caused by the different alkalinity of the catalysts as measured by CO$_2$-TPD (vide infra).

To determine the active sites of the cascade conversion process for the synthesis of **3a**, a series of control experiments were performed, involving the acceptorless dehydrogenation (Fig. 5c) and transfer hydrogenation (Fig. 5d) of the bio-alcohol **2a**. In general, SCN$^-$ can poison metal nanoparticles and cause inactivation, but not for porphyrin-like SACs [66]. This was also confirmed by our results that the activity of

Co$_{SAs}$/NC(0.08) after being poisoned by KSCN (20 equiv. of Co) did not decrease significantly. However, after poisoning Co$_{SAs-NPs}$/NC(0.25), the conversion of **1a** decreased by nearly 30%, and **3a** yield dropped by more than 45% (entries 7 & 8 in Table 2), with a certain amount of **5a** (18.9%) being detected, implying that Co-NPs facilitate nitro reduction. To evidence the effectiveness of different active sites for nitro hydrogenation, Co$_{NPs}$@C, Co$_{SAs}$/NC(0.08), and Co$_{SAs-NPs}$/NC(0.25) catalysts were investigated to synthesize **3a** from **2a** and **5a**. The dual-size
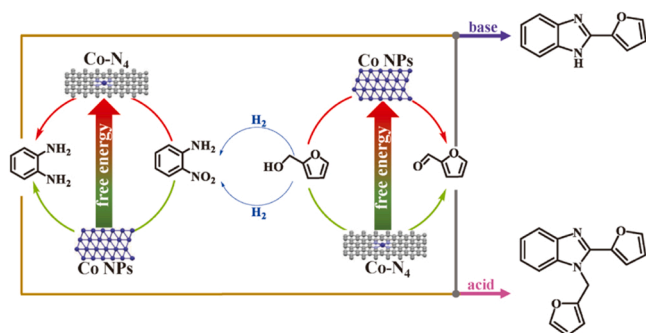
Fig. 7. The reaction routes to bio-based benzimidazoles with the main active sites of each process.

Co$_{SAs-NPs}$/NC(0.25) catalyst outperformed the Co$_{SAs}$/NC(0.08) and Co$_{NPs}$@C in terms of **5a** conversion, but none of these catalysts showed satisfactory selectivity toward **3a** (Fig. S15). It is speculated that the lack of necessary oxidation sites in the catalyst may lead to difficulty in the ring closure to give the target product [67]. In the acceptorless dehydrogenation experiment of **2a** and *o*-phenylenediamine (**1b**), the yield of Co$_{SAs}$/NC(0.08) was higher than those of Co$_{SAs-NPs}$/NC(0.25) (Fig. 5c), indicating that the Co-SAs show higher activity when the nitro group of the used substrate does not need to be reduced. The H$_2$ content in the reaction kettle gas was measured by GC with a thermal conductivity detector (TCD), and it was found that the amount of evolved hydrogen gas was 0.43 mmol when the Co$_{SAs}$/NC(0.08) catalyst was used. The stoichiometric ratio of hydrogen to converted furfuryl alcohol was about 1.6, which is basically consistent with the theoretical results. Therefore,

it can be considered that the Co-SAs have high activity in the dehydrogenation of the alcohol, while Co-NPs facilitate the reduction of the nitro group.

For nitrogen co-doped carbon-based catalysts with different metal particle sizes, they may show the SACs properties (M−N$_x$) after being etched by acid (e.g., HCl or HNO$_3$) [68,69]. Surprisingly, the main product obtained with the acid-etching catalyst (Co$_{SAs-NPs}$/NC(0.25) (HCl)) was 1,2-substituted benzimidazole (**4a**), while in the presence of Co$_{SAs}$/NC(0.08) 2-substituted benzimidazole (**3a**) is the major product (Fig. 5d). In addition, the products of Co$_{SAs-NPs}$/NC(0.5) and Co$_{SAs-NPs}$/NC(1) were dominated by **4a**, and the content of **4a** tended to increase with the decrease of Zn content (entry 5 & 6 in Table 2). After acid-etching the catalyst, most Co-NPs were washed away along with the ZnO that provided basic sites. The CO$_2$-TPD analysis suggests that the basicity of the catalyst decreases with the increase of Co content (Table 1). Given that the basicity of catalysts might affect the product distribution, weakly acidic ammonium chloride was added to the reaction system with Co$_{SAs-NPs}$/NC(0.25) as the catalyst. Compared to the system without ammonium chloride, **4a** in the product distribution tended to increase significantly, either the acceptorless dehydrogenation reaction with **1b** as the substrate (Fig. 5c) or the hydrogen transfer reaction with **1a** (Fig. 5d). Next, after adding a basic substance (KHCO$_3$) to Co$_{SAs-NPs}$/NC(1), the 2-substituted product (**3a**) increased obviously, while the 1,2-substituted product (**4a**) almost disappeared, with an overall increased product yield (Fig. 5d). This is mainly due to the fact that the basic sites can promote the nucleophilic addition reaction [38], resulting in the subsequent intramolecular cyclization to form the final heterocyclic compound. Overall, it is shown that the catalyst activity was enhanced under alkaline conditions with 2-substituted benzimidazole as the main product, but acidic conditions favor the formation of 1,
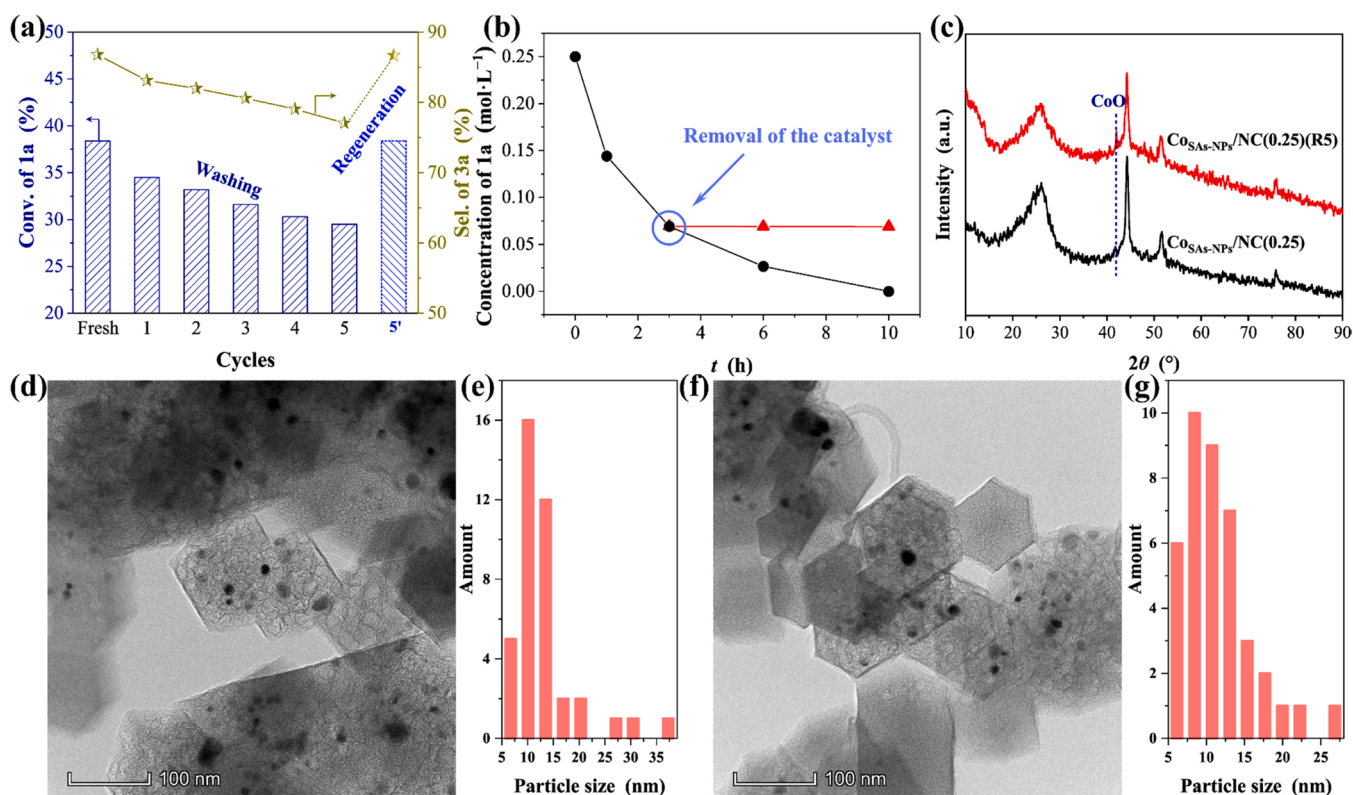

Fig. 8. (a) Reusability test of Co$_{SAs-NPs}$/NC(0.25) catalyst by abstersion and regeneration^a for the synthesis of **3a**. Note: The data is obtained at low **1a** conversions. (b) Hot-filtration experiment; The black and red lines indicate the concentration of **1a** without or after removal of the catalyst, respectively. (c) XRD patterns of Co$_{SAs-NPs}$/NC(0.25) and Co$_{SAs-NPs}$/NC(0.25)(R5). (d) TEM image of Co$_{SAs-NPs}$/NC(0.25). (e) Size distribution of Co-NPs on Co$_{SAs-NPs}$/NC(0.25). (f) TEM image of Co$_{SAs-NPs}$/NC(0.25) catalyst by regeneration^a. (g) Size distribution of Co-NPs on Co$_{SAs-NPs}$/NC(0.25) catalyst by regeneration^a. Reaction conditions: 0.025 mmol Co of catalyst, 0.5 mmol **1a**, 3 mmol **2a**, 150 °C, 1 h, 2 mL chlorobenzene.^{a}Regeneration conditions: Calcination at 400 °C for 2 h (heating rate: 5 °C·min^{-1}) in the atmosphere of 10% H$_2$/Ar (50 mL·min^{-1} of gas flow).
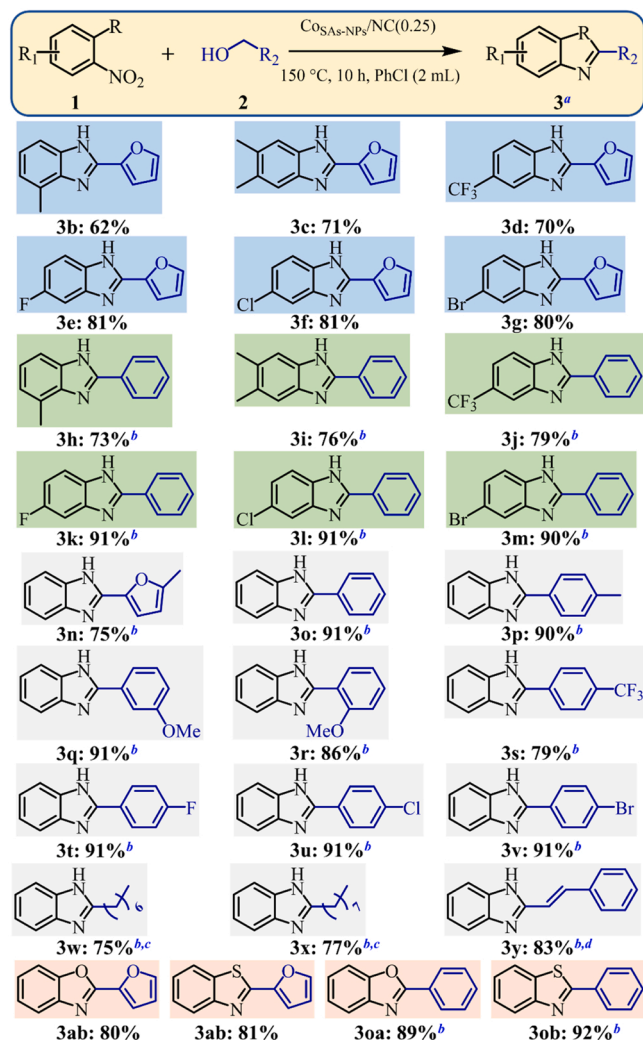
Fig. 9. Substrate scope study for synthesis of various benzimidazole derivatives. Reaction conditions: 0.025 mmol Co of catalyst, 0.5 mmol **1**, 3 mmol **2**, 150 °C, 10 h, 2 mL chlorobenzene. [a] Isolated yield. [b] 1.5 mmol benzyl alcohol or its derivative was used. [c] 1.0 mmol NH₄Cl, 24 h. [d] 24 h.

2-substituted benzimidazole.

3.3. Mechanism studies

In order to verify the influence of dual-size Co particles on the cascade conversion process, the free energy changes for the dehydrogenation of **2a** and the coupled hydrogenation of **1a** catalyzed by Co-SAs (i.e., CoN₄) and Co-NPs (i.e., Co(111)) sites were calculated by density functional theory (DFT) (Fig. 6). In the dehydrogenation process, **2a** is first adsorbed on the active sites (M1). The adsorption energy of **2a** at CoN₄ sites is − 0.85 eV, lower than that at Co(111) sites, indicating that Co-SAs improve the adsorption of **2a**. Subsequently, **2a** removes H* to generate the intermediate $C_5H_5O_2$ (M2). Then, the transition state (TS1) is formed by the removal of H* from the hydroxyl group of **2a**, and the energy barrier of CoN₄ (0.62 eV) is lower than that of Co(111) by 1.11 eV. Furfuryl alcohol was more dehydrogenated at the CoN₄ sites than benzyl alcohol (0.58 eV) [70], which also confirmed that the furfuryl intermediate was unstable compared to the benzyl intermediate. Likewise, the energy barrier of the second transition state (TS2) generated at the CoN₄ sites from M2 to the final product furfural (FS) is lower than at the Co(111) sites. It can be summarized that the CoN₄ sites are more efficient catalytically active sites for the dehydrogenation of **2a** compared with the Co(111) sites (Fig. 6a).

The DFT calculations on the reduction of **1a** to *o*-phenylenediamine (**1b**) were performed using CoN₄ and Co(111) as the catalytic sites (Fig. 6c). The first oxygen of the nitro group is activated by two H* followed by removal in the form of water, and then the second oxygen is removed through the same steps to finally give *o*-phenylenediamine (**1b**). For the initial hydrogenation of the first oxygen on the nitro group, the energy barrier from M2 to M3 on the CoN₄ sites is 0.73 eV (TS1), and the energy barrier for continued hydrogenation to form $C_6H_6N_2OOH_2$ (M5) is 0.36 eV (TS2). For the removal of the second oxygen on the nitro group, the two transition state energies that need to be overcome are both 0.62 eV (TS3, TS4). These barrier energies are higher than those required for the reduction of nitro groups at Co(111) sites (Fig. 6c). From the aspect of the total reaction, the free energy of Co (111) sites (−1.33 eV) is lower than that of CoN₄ (−0.60 eV), indicating that the reduction of nitro group catalyzed by the Co(111) sites is thermodynamically favored. In addition, the lower activated H* adsorption energy at the Co(111) site makes it easier to escape and participate in the process of nitro reduction (Fig. 6b and Fig. S16). Therefore, the reduction of **1a** occurs more easily at the Co(111) sites.

Combined with the above DFT calculation and experimental results, a feasible reaction pathway for transfer hydrogenative cyclization to synthesize bio-based benzimidazoles catalyzed by dual-size Co particles is shown in Fig. 7. Furfuryl alcohol (**2a**) undergoes dehydrogenation reaction under the Co-SAs sites to generate furfural, and 2-nitroaniline borrows the hydrogen from **2a**, followed by reduction to *o*-phenylenediamine (**1b**) under the action of Co-NPs and Co-SAs. Then the two intermediate products, *o*-phenylenediamine (**1b**) and furfural, undergo C−N coupling cyclization to rapidly generate 2-substituted benzimidazole in an alkaline local environment. Notably, the dominant product is 1,2-substituted benzimidazole in an acidic medium.

3.4. Catalyst reusability

Following the hydrogen transfer-dehydrogenative cyclization of **1a** with **2a**, the Co$_{SAs-NPs}$/NC(0.25) catalyst can be easily recuperated from the reaction mixture using an external magnet, with more than 95% recovery. After washing, the catalyst could be reused at least five times by keeping the same substrate-to-catalyst ratio, but its activity decreased with each reuse. After five batches of recycling, the **1a** conversion drops by no more than 10% (Fig. 8a). In addition, no further reaction was observed after filtering off the solid catalyst, suggesting a good heterogeneous behavior of the reaction system (Fig. 8b). To demonstrate the stability of the catalyst, a series of characterizations were carried out on the catalyst after five cycles (Co$_{SAs-NPs}$/NC(0.25)(R5)) and the fresh catalyst (Co$_{SAs-NPs}$/NC(0.25)). The results of the ICP-OES analysis showed that the Co content in the catalyst after the fifth cycle did not decrease significantly (Fig. S17), and both Co and Zn elements were not detected in the filtrate of the hot-filtration experiment, implying that the metal leaching was negligible. The TG results show that the weight loss curve had almost no change at all in the range of 800 °C between the fresh and reused (fifth cycle) catalysts, indicating that no product was adsorbed on the spent catalyst (Fig. S18). The XPS results display that the elemental species of the catalyst before and after use did not change (Fig. S19). The high-resolution Zn 2p XPS peak of the fresh catalyst was found to be consistent with that of the spent one (Fig. S20). XRD patterns illustrate that the diffraction peak position and intensity did not change after five cycles of the catalyst, and the three characteristic peaks of Co (111), Co(200), and Co(220) were still maintained (Fig. 8c). It is worth noting that a characteristic peak (JCPDS card: 72–1474) assigned to CoO appears at $2\theta = 42.6°$, implying that part of the metallic Co is oxidized to CoO. Similarly, the peak of Co 2p XPS of Co$_{SAs-NPs}$/NC(0.25)(R5) shifted to the vicinity of the Co−O bond banding energy (Fig. S21). After deconvolution of Co 2p XPS (Fig. S22), it was found that the relative content of Co⁰ in Co$_{SAs-NPs}$/NC(0.25)(R5) decreased from 9.74% to 6.50% (Fig. S17), which could cause the decrease of the catalyst activity and selectivity. Thus, the catalyst can be rejuvenated via reduction at

Table 3
Activity comparison of 2-nitroaniline (**1a**) and benzyl alcohol to synthesize substituted benzimidazoles.

Entry	2-Nitroaniline	Benzyl alcohol	Catalyst	Temp. (°C)	Time (h)	Yeild (%)	Additive	Ref.
1	0.5 mmol	1.0 mmol	Co(acac)$_2$ 5 mol%	135	24	73	^{t}BuONa (1 equiv)	[24]
2	2.5 mmol	3.75 mmol	FeCl$_3$·6 H$_2$O 1 mol%	130	24	95	Na$_2$S (0.4 equiv)	[25]
3	0.5 mmol	1.5 mmol	Knölker complex [Fe] 5 mol%	160	15	64	K$_3$PO$_4$ (1 equiv), Me$_3$NO (10 mol%)	[26]
4	0.4 mmol	0.6 mmol	Iron complexes Fe 2 mol%	150	42	80	^{t}BuONa (1.5 equiv) Me$_3$NO (4 mol%)	[27]
5	1 mmol	1 mmol	Cu-isatin Schiff base-g-Fe$_2$O$_3$ 1 mol%	100	15	82	KOH (1 mmol)	[28]
6	7.2 mmol	10.8 mmol	Ni(MeTAA) 3 mol%	120	24	62	^{t}BuOK (1 equiv)	[29]
7	1 mmol	2.5 mmol	dppf 0.05 mmol	150	24	74	no	[30]
8	58 mmol	120 mL	Cu−Pd/γ-Al$_2$O$_3$ 0.8 g	180	12	100	no	[31]
9	0.3 mmol	0.9 mmol	Pd(dppf)Cl$_2$ 0.015 mmol	160	24	97	no	[32]
10	1 mmol	4 mmol	Ir/TiO$_2$ 2.5 mol%	80	18	86	no	[33]
11	0.25 mmol	0.75 mmol	Au/TiO$_2$ 2 mol%	150	24	78	no	[34]
12	0.5 mmol	1.5 mmol	Co$_{SAs-NPs}$/NC(0.25) 0.025 mmol	150	7	87	no	This work

400 ºC in the presence of hydrogen (Fig. 8a). Obvious aggregation of Co-NPs was not observed by TEM on the regenerated catalyst, and the particle size distribution was between 5 and 30 nm, which was similar to the fresh catalyst (Fig. 8d-g). Therefore, upon treatment of the used catalyst to keep the Co-SAs and Co-NPs in a specific ratio, the Co$_{SAs-NPs}$/NC(0.25) catalyst can maintain good activity and excellent recyclability, further demonstrating the significant role of controlling the metal size in the synthesis of bio-based benzimidazoles via a cascade hydrogen transfer-dehydrogenative cyclization process.

3.5. Substrate scope

Inspired by the pronounced performance of Co$_{SAs-NPs}$/NC(0.25), the substrate scope for the synthesis of different substituted benzimidazoles was investigated (Fig. 9). By using this catalyst, the hydrogen transfer-dehydrogenative cyclization of **2a** with six 2-nitroaniline derivatives was developed for the preparation of bio-based benzimidazoles (Figs. 9, **3b-3g**). Sensitive functional groups, including alkyl and halogeno as well as challenging haloalkyl groups, were well tolerated. Compared with furfuryl alcohol (**2a**), benzyl alcohol used as H-donor and reactant could afford a higher product yield at a relatively lower molar concentration due to the formation of a more stable intermediate in hydrogen transfer reaction (**3h-3m**). It was found that 2-nitroaniline could be wholly converted when adding more than three equivalents of benzyl alcohol, but excess benzyl alcohol would reduce the selectivity of 2-substituted benzimidazoles (Fig. S23). Therefore, three equivalents of benzyl alcohol and its derivatives were selected to study the range of substrates. When the substituents of 2-nitroaniline derivatives are alkyl and haloalkyl groups, it may be affected by steric hindrance, and the product yield is between 73% and 79% (**3h-3j**). While changing the substituent to halogen, the product yield can be maintained above 90% (**3k-3m**). Furthermore, the reaction of **1a** with different substituted furyl/aryl alcohols was investigated under optimal reaction conditions. They showed good (75%) to excellent (91%) yields for both electron-donating substrates and electron-withdrawing substrates (**3n-3v**). Also, aliphatic alcohols (e.g., 1-octanol and 1-nonanol) and allyl alcohols (e.g., cinnamyl alcohol) were used as substrates for the synthesis of benzimidazoles in moderate yields (75%−83%) under the further optimized reaction conditions (**3w-3y**). Finally, the substrates were expanded to access benzothiazoles and benzoxazoles and the yields of

these products were comparable to the corresponding benzimidazoles (**3aa**, **3ab**, **3oa**, and **3ob**), indicating that the dual-size catalyst has good substrate universality. The above experimental results show that the yield of substituted benzimidazoles in this catalytic system is mainly affected by the steric hindrance of the substrate, and all have good tolerance to sensitive functional groups. On the whole, the dual-size heterogeneous N-doped cobalt catalyst is widely applicable to the synthesis of 2-substituted benzimidazoles from bio-alcohols via a cascade conversion process in one pot.

3.6. Activity comparison

The activity of different metal catalysts reported in the literature was compared with our developed Co$_{SAs-NPs}$/NC(0.25) catalyst using benzyl alcohol as the substrate (Table 3). It can be seen that when non-noble metals are used as catalysts, exogenous basic additives are required in the literature, which is not conducive to the concept of green chemistry. Meanwhile, these catalysts either exist in the form of homogeneous metal salts [24,25] or use expensive complex organic ligands [26–30]. Noble metal catalysts can also obtain higher yields without any additives [31–34]. In this work, the Co$_{SAs-NPs}$/NC(0.25) catalyst has high yields at a moderate temperature for a short time without any additives, indicating that the developed catalyst Co$_{SAs-NPs}$/NC(0.25) has a satisfactory yield comparable to that of noble metals (Table 3).

4. Conclusions

In summary, the integration of high content of Co-SAs and high dispersion of Co-NPs was realized in a single heterogenous Co catalyst, which shows good performance in the cascade conversion process of hydrogen transfer-dehydrogenative cyclization to synthesize bio-based benzimidazoles. Control experiments show that the cascade reaction was remarkably enhanced by the synergistic effect to obtain superior selectivity toward 2-substituted benzimidazoles. It was found that atomically dispersed Co has higher activity in the dehydrogenation of the bio-alcohol, while Co-NPs can promote the reduction of 2-nitroaniline. DFT calculations explicitly elaborated that the energy barrier to be overcome at the CoN$_4$ sites (Co-SAs) in the bio-alcohol dehydrogenation was low, and the free energy (−1.33 eV) of the Co(111) sites (Co-NPs) in the nitro reduction reaction was lower than that of CoN$_4$

(−0.60 eV). In addition, the alkalinity of the catalyst plays an important role in the product distribution for the production of the substituted benzimidazoles. Besides, the Co catalyst containing Co-SAs and Co-NPs exhibited good reusability and high tolerance of sensitive functional groups in a wide range of substrates. This study not only provides the possibility for the synthesis of various benzimidazole derivatives, but also contributes to developing a dual-size metal catalytic strategy for the valorization of biomass and its derivates.

CRediT authorship contribution statement

Baoyu Wang: Methodology, Formal analysis, Investigation, Writing – review & editing. **Mingrui Li:** Investigation. **Songdang Zhang:** Formal analysis. **Hongguo Wu:** Methodology. **Yuhe Liao:** Writing – review & editing. **Hu Li:** Supervision, Conceptualization, Methodology, Writing – review & editing.

Declaration of Competing Interest

The authors declare that they have no known competing financial interests or personal relationships that could have appeared to influence the work reported in this paper.

Data Availability

Data will be made available on request.

Acknowledgments

Appendix A. Supporting information

Supplementary data associated with this article can be found in the online version at doi:10.1016/j.apcatb.2023.122454.

References

[1] C. Xu, E. Paone, D. Rodríguez-Padrón, R. Luque, F. Mauriello, Recent catalytic routes for the preparation and the upgrading of biomass derived furfural and 5-hydroxymethylfurfural, Chem. Soc. Rev. 49 (2020) 4273–4306, https://doi.org/10.1039/d0cs00041h.

[2] P. Sudarsanam, E. Peeters, E.V. Makshina, V.I. Parvulescu, B.F. Sels, Advances in porous and nanoscale catalysts for viable biomass conversion, Chem. Soc. Rev. 48 (2019) 2366–2421, https://doi.org/10.1039/c8cs00452h.

[3] S. Chen, R. Wojcieszak, F. Dumeignil, E. Marceau, S. Royer, How catalysts and experimental conditions determine the selective hydroconversion of furfural and 5-hydroxymethylfurfural, Chem. Rev. 118 (2018) 11023–11117, https://doi.org/10.1021/acs.chemrev.8b00134.

[4] J. Iglesias, I. Martínez-Salazar, P. Maireles-Torres, D. Martin Alonso, R. Mariscal, M. López Granados, Advances in catalytic routes for the production of carboxylic acids from biomass: a step forward for sustainable polymers, Chem. Soc. Rev. 49 (2020) 5704–5771, https://doi.org/10.1039/d0cs00177e.

[5] C. Espro, E. Paone, F. Mauriello, R. Gotti, E. Uliassi, M.L. Bolognesi, D. Rodríguez-Padrón, R. Luque, Sustainable production of pharmaceutical, nutraceutical and bioactive compounds from biomass and waste, Chem. Soc. Rev. 50 (2021) 11191–11207, https://doi.org/10.1039/d1cs00524c.

[6] E.T. Hennessy, T.A. Betley, Complex N-heterocycle synthesis via iron-catalyzed, direct C−H bond amination, Science 340 (2013) 591–595, https://doi.org/10.1126/science.1233701.

[7] Y. Wang, W.X. Zhang, Z. Xi, Carbodiimide-based synthesis of N-heterocycles: moving from two classical reactive sites to chemical bond breaking/forming reaction, Chem. Soc. Rev. 49 (2020) 5810–5849, https://doi.org/10.1039/c9cs00478e.

[8] M. Pelckmans, T. Renders, S. Van de Vyver, B.F. Sels, Bio-based amines through sustainable heterogeneous catalysis, Green. Chem. 19 (2017) 5303–5331, https://doi.org/10.1039/c7gc02299a.

[9] H. Li, H. Guo, Z. Fang, T.M. Aida, R.L. Smith, Cycloamination strategies for renewable N-heterocycles, Green. Chem. 22 (2020) 582–611, https://doi.org/10.1039/c9gc03655e.

[10] Y. Li, X. Zhou, H. Wu, Z. Yu, H. Li, S. Yang, Nanospheric heterogeneous acid-enabled direct upgrading of biomass feedstocks to novel benzimidazoles with potent antibacterial activities, Ind. Crop. Prod. 150 (2020), 112406, https://doi.org/10.1016/j.indcrop.2020.112406.

[11] C.S.W. Law, K.Y. Yeong, Benzimidazoles in drug discovery: a patent review, ChemMedChem 16 (2021) 1861–1877, https://doi.org/10.1002/cmdc.202100004.

[12] L. Chen, Y. Zhang, Y. Zhou, G.H. Li, X.S. Feng, Pretreatment and determination methods for benzimidazoles: an update since 2005, J. Chromatogr. A 1644 (2021), 462068, https://doi.org/10.1016/j.chroma.2021.462068.

[13] Z. Li, H. Song, R. Guo, M. Zuo, C. Hou, S. Sun, X. He, Z. Sun, W. Chu, Visible-light-induced condensation cyclization to synthesize benzimidazoles using fluorescein as a photocatalyst, Green. Chem. 21 (2019) 3602–3605, https://doi.org/10.1039/c9gc01359h.

[14] Z. Ye, J. Chen, Sulfonate-grafted metal–organic frameworks for reductive functionalization of CO_2 to benzimidazoles and *N*-formamides, ACS Catal. 11 (2021) 13983–13999, https://doi.org/10.1021/acscatal.1c03329.

[15] D. Raja, A. Philips, P. Palani, W.Y. Lin, S. Devikala, G.C. Senadi, Metal-free synthesis of benzimidazoles via oxidative cyclization of D-glucose with o-phenylenediamines in water, J. Org. Chem. 85 (2020) 11531–11540, https://doi.org/10.1021/acs.joc.0c01053.

[16] Y. Qin, M. Hao, M. Cu, Z. Li, Visible light initiated oxidative coupling of alcohols and o-phenylenediamines to synthesize benzimidazoles over MIL-101(Fe) promoted by plasmonic Au, Green. Chem. 23 (2021) 4161–4169, https://doi.org/10.1039/d1gc01047f.

[17] K. Das, A. Mondal, D. Srimani, Selective synthesis of 2-substituted and 1,2-disubstituted benzimidazoles directly from aromatic diamines and alcohols catalyzed by molecularly defined nonphosphine manganese(I) complex, J. Org. Chem. 83 (2018) 9553–9560, https://doi.org/10.1021/acs.joc.8b01316.

[18] M. Maji, D. Panja, I. Borthakur, S. Kundu, Recent advances in sustainable synthesis of N-heterocycles following acceptorless dehydrogenative coupling protocol using alcohols, Org. Chem. Front. 8 (2021) 2673–2709, https://doi.org/10.1039/d0qo01577f.

[19] H. Li, Y. Zhang, Z. Yan, Z. Lai, R. Yang, M. Peng, Y. Sun, J. An, Methanol as the C_1 source: redox coupling of nitrobenzenes and alcohols for the synthesis of benzimidazoles, Green. Chem. 24 (2022) 748–753, https://doi.org/10.1039/d1gc03907e.

[20] C. Lin, W. Wan, X. Wei, J. Chen, H_2 activation with Co nanoparticles encapsulated in N-doped carbon nanotubes for green synthesis of benzimidazoles, ChemSusChem 14 (2021) 709–720, https://doi.org/10.1002/cssc.202002344.

[21] L. Hao, Y. Zhao, B. Yu, H. Zhang, H. Xu, Z. Liu, Au catalyzed synthesis of benzimidazoles from 2-nitroanilines and CO_2/H_2, Green. Chem. 16 (2014) 3039–3044, https://doi.org/10.1039/c4gc00153b.

[22] B.G. Reed-Berendt, D.E. Latham, M.B. Dambatta, L.C. Morrill, Borrowing hydrogen for organic synthesis, ACS Cent. Sci. 7 (2021) 570–585, https://doi.org/10.1021/acscentsci.1c00125.

[23] T. Irrgang, R. Kempe, 3d-Metal catalyzed N- and C-alkylation reactions via borrowing hydrogen or hydrogen autotransfer, Chem. Rev. 119 (2019) 2524–2549, https://doi.org/10.1021/acs.chemrev.8b00306.

[24] S. Das, S. Mallick, S. De Sarkar, Cobalt-catalyzed sustainable synthesis of benzimidazoles by redox-economical coupling of o-nitroanilines and alcohols, J. Org. Chem. 84 (2019) 12111–12119, https://doi.org/10.1021/acs.joc.9b02090.

[25] A. Al-Mourabit, T.B. Nguyen, L. Ermolenko, Sodium sulfide: A sustainable solution for unbalanced redox condensation reaction between o-nitroanilines and alcohols catalyzed by an iron–sulfur system, Synthesis 47 (2015) 1741–1748, https://doi.org/10.1055/s-0034-1380134.

[26] J. Wu, C. Darcel, Iron-catalyzed hydrogen transfer reduction of nitroarenes with alcohols: Synthesis of imines and aza heterocycles, J. Org. Chem. 86 (2021) 1023–1036, https://doi.org/10.1021/acs.joc.0c02505.

[27] R.R. Putta, S. Chun, S.H. Choi, S.B. Lee, D.C. Oh, S. Hong, Iron(0)-catalyzed transfer hydrogenative condensation of nitroarenes with alcohols: A straightforward approach to benzoxazoles, benzothiazoles, and benzimidazoles, J. Org. Chem. 85 (2020) 15396–15405, https://doi.org/10.1021/acs.joc.0c02191.

[28] S. Sobhani, H.H. Moghadam, S.R. Derakhshan, J.M. Sansano, Tandem imine formation via auto-hydrogen transfer from alcohols to nitro compounds catalyzed by a nanomagnetically recyclable copper catalyst under solvent-free conditions, RSC Adv. 11 (2021) 19121–19127, https://doi.org/10.1039/d1ra02347k.

[29] G. Chakraborty, R. Mondal, A.K. Guin, N.D. Paul, Nickel catalyzed sustainable synthesis of benzazoles and purines via acceptorless dehydrogenative coupling and borrowing hydrogen approach, Org. Biomol. Chem. 19 (2021) 7217–7233, https://doi.org/10.1039/d1ob01154e.

[30] G. Li, J. Wang, B. Yuan, D. Zhang, Z. Lin, P. Li, H. Huang, Iron-catalyzed one-pot synthesis of benzimidazoles from 2-nitroanilines and benzylic alcohols, Tetrahedron Lett. 54 (2013) 6934–6936, https://doi.org/10.1016/j.tetlet.2013.10.045.

[31] F. Feng, J. Ye, Z. Cheng, X. Xu, Q. Zhang, L. Ma, C. Lu, X. Li, Cu–Pd/γ-Al$_2$O$_3$ catalyzed the coupling of multi-step reactions: direct synthesis of benzimidazole derivatives, RSC Adv. 6 (2016) 72750–72755, https://doi.org/10.1039/c6ra13004f.

[32] X. Li, R. Hu, Y. Tong, Q. Pan, D. Miao, S. Han, An efficient route for the synthesis of benzimidazoles via a hydrogen-transfer strategy between *o*-nitroanilines and alcohols, Tetrahedron Lett. 57 (2016) 4645–4649, https://doi.org/10.1016/j.tetlet.2016.09.018.

[33] T. Fukutake, K. Wada, H. Yu, S. Hosokawa, Q. Feng, Development of titania-supported iridium catalysts with excellent low-temperature activities for the synthesis of benzimidazoles via hydrogen transfer, Mol. Catal. 477 (2019) 110550, https://doi.org/10.1016/j.mcat.2019.110550.

[34] L. Tang, X. Guo, Y. Yang, Z. Zha, Z. Wang, Gold nanoparticles supported on titanium dioxide: an efficient catalyst for highly selective synthesis of benzoxazoles and benzimidazoles, Chem. Commun. 50 (2014) 6145–6148, https://doi.org/10.1039/c4cc01822b.

[35] X. Cui, Z. Huang, A.P. van Muyden, Z. Fei, T. Wang, P.J. Dyson, Acceptorless dehydrogenation and hydrogenation of N- and O-containing compounds on Pd$_3$Au$_1$(111) facets, Sci. Adv. 6 (2020) eabb3831, https://doi.org/10.1126/sciadv.abb3831.

[36] T. Wang, J. Sha, M. Sabbe, P. Sautet, M. Pera-Titus, C. Michel, Identification of active catalysts for the acceptorless dehydrogenation of alcohols to carbonyls, Nat. Commun. 12 (2021) 5100, https://doi.org/10.1038/s41467-021-25214-1.

[37] F. Cai, Y. Guo, J.J. Ibrahim, J. Zhang, Y. Sun, A highly active and stable Pd/MoC catalyst for hydrogen production from methanol decomposition, Appl. Catal. B 299 (2021), 120648, https://doi.org/10.1016/j.apcatb.2021.120648.

[38] Q. Xu, Q. Li, X. Zhu, J. Chen, Green and scalable aldehyde-catalyzed transition metal-free dehydrative *N*-alkylation of amides and amines with alcohols, Adv. Synth. Catal. 355 (2013) 73–80, https://doi.org/10.1002/adsc.201200881.

[39] C. Vogt, B.M. Weckhuysen, The concept of active site in heterogeneous catalysis, Nat. Rev. Chem. 6 (2022) 89–111, https://doi.org/10.1038/s41570-021-00340-y.

[40] R. Jin, G. Li, S. Sharma, Y. Li, X. Du, Toward active-site tailoring in heterogeneous catalysis by atomically precise metal nanoclusters with crystallographic structures, Chem. Rev. 121 (2021) 567–648, https://doi.org/10.1021/acs.chemrev.0c00495.

[41] M. Hao, Z. Li, Efficient visible light initiated one-pot syntheses of secondary amines from nitro aromatics and benzyl alcohols over Pd@NH$_2$-UiO-66(Zr), Appl. Catal. B 305 (2022), 121031, https://doi.org/10.1016/j.apcatb.2021.121031.

[42] Y. Xin, K. Yu, L. Zhang, Y. Yang, H. Yuan, H. Li, L. Wang, J. Zeng, Copper-based plasmonic catalysis: Recent advances and future perspectives, Adv. Mater. 33 (2021) 2008145, https://doi.org/10.1002/adma.202008145.

[43] M.A. Salaev, A.A. Salaeva, T.S. Kharlamova, G.V. Mamontov, Pt-CeO$_2$-based composites in environmental catalysis: a review, Appl. Catal. B 295 (2021), 120286, https://doi.org/10.1016/j.apcatb.2021.120286.

[44] R.V. Jagadeesh, K. Murugesan, A.S. Alshammari, H. Neumann, M.M. Pohl, J. Radnik, M. Beller, MOF-derived cobalt nanoparticles catalyze a general synthesis of amines, Science 358 (2017) 326–332, https://doi.org/10.1126/science.aan6245.

[45] P. Duan, J. Pan, W. Du, Q. Yue, B. Gao, X. Xu, Activation of peroxymonosulfate via mediated electron transfer mechanism on single-atom Fe catalyst for effective organic pollutants removal, Appl. Catal. B 299 (2021) 120714, https://doi.org/10.1016/j.apcatb.2021.120714.

[46] Y. Han, Y.G. Wang, W. Chen, R. Xu, L. Zheng, J. Zhang, J. Luo, R.A. Shen, Y. Zhu, W.C. Cheong, C. Chen, Q. Peng, D. Wang, Y. Li, Hollow N-doped carbon spheres with isolated cobalt single atomic sites: Superior electrocatalysts for oxygen reduction, J. Am. Chem. Soc. 139 (2017) 17269–17272, https://doi.org/10.1021/jacs.7b10194.

[47] Y. Kamei, Y. Seino, Y. Yamaguchi, T. Yoshino, S. Maeda, M. Kojima, S. Matsunaga, Silane- and peroxide-free hydrogen atom transfer hydrogenation using ascorbic acid and cobalt-photoredox dual catalysis, Nat. Commun. 12 (2021) 966, https://doi.org/10.1038/s41467-020-20872-z.

[48] Q. Shen, H. Jin, P. Li, X. Yu, L. Zheng, W. Song, C. Cao, Breaking the activity limitation of iridium single-atom catalyst in hydrogenation of quinoline with synergistic nanoparticles catalysis, Nano Res. 15 (2022) 5024–5031, https://doi.org/10.1007/s12274-022-4235-4.

[49] H. Jeong, S. Shin, H. Lee, Heterogeneous atomic catalysts overcoming the limitations of single-atom catalysts, ACS Nano 14 (2020) 14355–14374, https://doi.org/10.1021/acsnano.0c06610.

[50] T.N. Ye, Z. Xiao, J. Li, Y. Gong, H. Abe, Y. Niwa, M. Sasase, M. Kitano, H. Hosono, Stable single platinum atoms trapped in sub-nanometer cavities in 12CaO·7Al$_2$O$_3$ for chemoselective hydrogenation of nitroarenes, Nat. Commun. 11 (2020) 1020, https://doi.org/10.1038/s41467-019-14216-9.

[51] T. Shen, X. Huang, S. Xi, W. Li, S. Sun, Y. Hou, The ORR electron transfer kinetics control via Co-N$_x$ and graphitic N sites in cobalt single atom catalysts in alkaline and acidic media, J. Energy Chem. 68 (2022) 184–194, https://doi.org/10.1016/j.jechem.2021.10.027.

[52] D. Saliba, M. Ammar, M. Rammal, M. Al-Ghoul, M. Hmadeh, Crystal growth of ZIF-8, ZIF-67, and their mixed-metal derivatives, J. Am. Chem. Soc. 140 (2018) 1812–1823, https://doi.org/10.1021/jacs.7b11589.

[53] F. Hillman, J.M. Zimmerman, S.M. Paek, M.R.A. Hamid, W.T. Lim, H.K. Jeong, Rapid microwave-assisted synthesis of hybrid zeolitic–imidazolate frameworks with mixed metals and mixed linkers, J. Mater. Chem. A 5 (2017) 6090–6099, https://doi.org/10.1039/c6ta11170j.

[54] J. Tang, R.R. Salunkhe, J. Liu, N.L. Torad, M. Imura, S. Furukawa, Y. Yamauchi, Thermal conversion of core-shell metal-organic frameworks: a new method for selectively functionalized nanoporous hybrid carbon, J. Am. Chem. Soc. 137 (2015) 1572–1580, https://doi.org/10.1021/ja511539a.

[55] J. Yang, F. Zhang, H. Lu, X. Hong, H. Jiang, Y. Wu, Y. Li, Hollow Zn/Co ZIF particles derived from core-shell ZIF-67@ZIF-8 as selective catalyst for the semi-hydrogenation of acetylene, Angew. Chem. Int. Ed. 54 (2015) 10889–10893, https://doi.org/10.1002/anie.201504242.

[56] T.E. Westre, P. Kennepohl, J.G. DeWitt, B. Hedman, K.O. Hodgson, E.I. Solomon, A multiplet analysis of Fe K-edge 1s → 3d pre-edge features of iron complexes, J. Am. Chem. Soc. 119 (1997) 6297–6314, https://doi.org/10.1021/ja964352a.

[57] Z. Miao, W. Liu, Y. Zhao, F. Wang, J. Meng, M. Liang, X. Wu, J. Zhao, S. Zhuo, J. Zhou, Zn-Modified Co@N–C composites with adjusted Co particle size as catalysts for the efficient electroreduction of CO$_2$, Catal. Sci. Technol. 10 (2020) 967–977, https://doi.org/10.1039/c9cy02203a.

[58] Z. Chen, R. Wu, Y. Liu, Y. Ha, Y. Guo, D. Sun, M. Liu, F. Fang, Ultrafine Co nanoparticles encapsulated in carbon-nanotubes-grafted graphene sheets as advanced electrocatalysts for the hydrogen evolution reaction, Adv. Mater. 30 (2018) 1802011, https://doi.org/10.1002/adma.201802011.

[59] J. Meng, C. Niu, L. Xu, J. Li, X. Liu, X. Wang, Y. Wu, X. Xu, W. Chen, Q. Li, Z. Zhu, D. Zhao, L. Mai, General oriented formation of carbon nanotubes from metal-organic frameworks, J. Am. Chem. Soc. 139 (2017) 8212–8221, https://doi.org/10.1021/jacs.7b01942.

[60] D.H. Guo, R. Shibuya, C. Akiba, S. Saji, T. Kondo, J. Nakamura, Active sites of nitrogen-doped carbon materials for oxygen reduction reaction clarified using model catalysts, Science 351 (2016) 361–365, https://doi.org/10.1126/science.aad0832.

[61] Z. Geng, X. Kong, W. Chen, H. Su, Y. Liu, F. Cai, G. Wang, J. Zeng, Oxygen vacancies in ZnO nanosheets enhance CO$_2$ electrochemical reduction to CO, Angew. Chem. Int. 57 (2018) 6054–6059, https://doi.org/10.1002/anie.201711255.

[62] B. Li, X. Sun, D. Su, Calibration of the basic strength of the nitrogen groups on the nanostructured carbon materials, Phys. Chem. Chem. Phys. 17 (2015) 6691–6694, https://doi.org/10.1039/c4cp05765a.

[63] B. Liu, T. Fang, Y. He, In–Co–Zn/C–N catalysts derived from ZIFs for selective hydrogenation of CO$_2$ into methanol, Catal. Sci. Technol. 12 (2022) 300–309, https://doi.org/10.1039/d1cy01663f.

[64] J.N. Appaturi, J. Andas, Solid catalysts for furfuryl alcohol conversion to drop-in chemicals, in: P. Sudarsanam, H. Li (Eds.), Advanced Catalysis for Drop-in Chemicals, Elsevier, Inc, Amsterdam, 2022, pp. 291–311, https://doi.org/10.1016/B978-0-12-823827-1.00011-0.

[65] K. Sun, H. Shan, G.P. Lu, C. Cai, M. Beller, Synthesis of *N*-heterocycles via oxidant-free dehydrocyclization of alcohols using heterogeneous catalysts, Angew. Chem. Int. Ed. 60 (2021) 25188–25202, https://doi.org/10.1002/anie.202104979.

[66] X. Wang, D. Xia, Y. Zhang, H. Du, F. Kang, L. Gan, J. Li, Unveiling the axial hydroxyl ligand on Fe–N$_4$–C electrocatalysts and its impact on the pH-dependent oxygen reduction activities and poisoning kinetics, Adv. Sci. 7 (2020) 2000176, https://doi.org/10.1002/advs.202000176.

[67] D. Xue, Y.Q. Long, Metal-free TEMPO-promoted C(sp^3)−H amination to afford multisubstituted benzimidazoles, J. Org. Chem. 79 (2014) 4727–4734, https://doi.org/10.1021/jo5005179.

[68] M. Li, S. Chen, Q. Jiang, Q. Chen, X. Wang, Y. Yan, J. Liu, C. Lv, W. Ding, X. Guo, Origin of the activity of Co–N–C catalysts for chemoselective hydrogenation of nitroarenes, ACS Catal. 11 (2021) 3026–3039, https://doi.org/10.1021/acscatal.0c05479.

[69] C. Wang, H. Ren, Z. Wang, Q. Guan, Y. Liu, W. Li, A promising single-atom Co−N−C catalyst for efficient CO$_2$ electroreduction and high-current solar conversion of CO$_2$ to CO, Appl. Catal. B 304 (2022), 120958, https://doi.org/10.1016/j.apcatb.2021.120958.

[70] C. Liu, T. Li, X. Dai, J. Zhao, D. He, G. Li, B. Wang, X. Cui, Catalytic activity enhancement on alcohol dehydrogenation via directing reaction pathways from single- to double-atom catalysis, J. Am. Chem. Soc. 144 (2022) 4913–4924, https://doi.org/10.1021/jacs.1c12705.